






Time Variations of the Nonpotential and Volume-threading Magnetic Helicities

L. Linan¹, É. Pariat¹ , K. Moraitis¹, G. Valori² , and J. Leake³ 

¹ LESIA, Observatoire de Paris, Université PSL, CNRS, Sorbonne Université, Univ. Paris Diderot, Sorbonne Paris Cité, 5 place Jules Janssen, F-92195 Meudon, France; luis.linan@obspm.fr

² Mullard Space Science Laboratory, University College London, Holmbury St. Mary, Dorking, Surrey, RH5 6NT, UK

³ NASA Goddard Space Flight Center, 8800 Greenbelt Road, Greenbelt, MD, 22071, USA

Received 2018 July 3; revised 2018 August 14; accepted 2018 August 14; published 2018 September 20

Abstract

Relative magnetic helicity is a gauge-invariant quantity suitable for the study of the magnetic helicity content of heliospheric plasmas. Relative magnetic helicity can be decomposed uniquely into two gauge-invariant quantities, the magnetic helicity of the nonpotential component of the field and a complementary volume-threading helicity. Recent analysis of numerical experiments simulating the generation of solar eruptions have shown that the ratio of the nonpotential helicity to the total relative helicity is a clear marker of the eruptivity of the magnetic system, and that the high value of that quantity could be a sufficient condition for the onset of the instability generating the eruptions. The present study introduces the first analytical examination of the time variations of these nonpotential and volume-threading helicities. The validity of the analytical formulae derived are confirmed with analysis of 3D magnetohydrodynamics (MHD) simulations of solar coronal dynamics. Both the analytical investigation and the numerical application show that, unlike magnetic helicity, the nonpotential and the volume-threading helicities are not conserved quantities, even in the ideal MHD regime. A term corresponding to the transformation between the nonpotential and volume-threading helicities frequently dominates their dynamics. This finding has an important consequence for their estimation in the solar corona: unlike with relative helicity, their volume coronal evolution cannot be ascertained by the flux of these quantities through the volume's boundaries. Only techniques extrapolating the 3D coronal field will enable both the proper study of the nonpotential and volume-threading helicities and the observational analysis of helicity-based solar-eruptivity proxies.

Key words: magnetic fields – Sun: corona – Sun: flares – Sun: photosphere

1. Introduction

Magnetic helicity was originally introduced by Elsässer (1956) as a volume integral related to the 3D distribution of the magnetic field. Moffatt (1969) provided a physical interpretation of this integral, showing that it was intimately related to the Gauss linking number and hence that magnetic helicity quantitatively describes the level of entanglement of magnetic field lines in a magnetized plasma. Magnetic helicity is of particular interest within the ideal magnetohydrodynamic (MHD) paradigm, as it is a strictly conserved quantity (Woltjer 1958); creation or dissipation of helicity is forbidden, and helicity can only be transported. From observations of the dynamics of plasmas in tokamak experiments, Taylor (1974) conjectured that even in nonideal MHD the dissipation of magnetic helicity should be relatively weak. Pariat et al. (2015) recently presented numerical evidence that magnetic helicity is indeed very well conserved, even when strong nonideal effects such as those associated with solar eruptions develop. Thanks to this conservation property, physical quantities based on magnetic helicity are increasingly studied in natural plasmas where the MHD paradigm applies, e.g., in solar/stellar interiors and atmosphere, as well as solar/stellar winds (Miesch et al. 2016; Valori et al. 2016; Brandenburg et al. 2017).

In the solar context, the conservation of magnetic helicity provides a natural explanation for the existence of ejecta transporting away excess magnetic helicity that cannot indefinitely accumulate in the solar atmosphere; coronal mass ejections (CMEs) and magnetic clouds and their underlying twisted magnetic structures (e.g., Burlaga 1995; Démoulin 2008) appear to be the necessary consequence of magnetic helicity conservation (Rust 1994; Low 1996).

Magnetic helicity and its conservation are a topic of study when trying to link solar eruptions, CMEs, and their interplanetary counterparts (Dasso et al. 2003, 2005; Luoni et al. 2005; Mandrini et al. 2005; Dasso 2009; Hu et al. 2014; Démoulin et al. 2016; Patsourakos et al. 2016; Patsourakos & Georgoulis 2017). Magnetic helicity conservation is also invoked as an essential element that impacts the dynamics of magnetic reconnection (e.g., Linton et al. 2001; Linton & Antiochos 2002; Del Sordo et al. 2010), solar/stellar dynamos (e.g., Brandenburg & Subramanian 2005; Candelaresi 2012), the formation of solar filaments (e.g., Antiochos 2013; Knizhnik et al. 2015; Zhao et al. 2015), and the generation of solar eruptions (e.g., Kusano et al. 2004; Longcope & Beveridge 2007; Priest et al. 2016). Because of this hypothesis, important efforts to estimate the magnetic helicity in the solar coronal have been carried out over the past decades (Démoulin 2007; Démoulin & Pariat 2009; Valori et al. 2016).

Because of the physical requirement of gauge transformation invariance, Elsässer's magnetic helicity can generally not be used to study natural plasmas. Berger & Field (1984) and Finn & Antonsen (1985) introduced a gauge-invariant quantity related to magnetic helicity that can be practically used with natural plasmas: the relative magnetic helicity. The direct estimation of relative helicity requires knowledge of the full distribution in the 3D volume studied, while state-of-the-art solar observations only provide measurements on a 2D surface, the solar photosphere. Estimation of relative helicity by volume integration is thus model dependent and requires 3D extrapolation of the magnetic field. A few methods estimating relative magnetic helicity (Rudenko & Myshyakov 2011;

Thalmann et al. 2011; Valori et al. 2012; Yang et al. 2013) by such volume integration have been recently developed and benchmarked (see review by Valori et al. 2016), enabling their use to study observed solar active regions (Valori et al. 2013; Moraitis et al. 2014; Guo et al. 2017; Polito et al. 2017; Temmer et al. 2017; James et al. 2018).

Because of the inherent observational difficulty of measuring helicity from volume integration, alternative methods have been developed (e.g. Démoulin et al. 2006; Longcope et al. 2007; Kazachenko et al. 2009, 2010, 2012; Guo et al. 2010, 2013, 2017; Georgoulis et al. 2012) that rely on an implicit model of the solar coronal field. However, the historically most commonly used method to evaluate magnetic helicity relies on the calculation of the flux of helicity through the solar photosphere and the time integration of this flux to obtain the helicity that accumulates into the corona. This approach was originally developed by Chae (2001) and has received further improvements (Pariat et al. 2005; Chae 2007; Liu & Schuck 2012, 2013; Dalmasse et al. 2014, 2018). This method does not make any specific assumption about the coronal magnetic field. It does, however, heavily rely on the helicity conservation principle since it assumes that the time-accumulated boundary flux of helicity is a good approximation of the volume helicity, with the coronal helicity dissipation being null and its ejection through eruptions negligible, at least during the formation phase of active regions.

Relative helicity is not the only magnetic-helicity-based quantity that has been studied. Berger (1985) used a formulation of magnetic helicity and relative magnetic helicity where the magnetic field is decomposed into poloidal and toroidal components. Consistent with this approach, Low (2006) introduced the primitive helicity in a two-flux description in which the field is represented by Euler potentials. These examples of the linear decomposition of a magnetic field into the sum of untwisted fields respect the requirement of gauge independence and easily allow the establishment of the helicity transport equation in Lagrangian variables (Webb et al. 2010, 2011).

Berger (2003) also showed that magnetic helicity can be decomposed into two gauge-invariant quantities, the current-carrying magnetic helicity and the volume-threading helicity. To our knowledge, Moraitis et al. (2014) were the first to estimate and follow these quantities. In the numerical simulations of the formation of an active region that they analyzed, the current-carrying helicity exhibited large fluctuations around the onset of eruptions. Recently, Pariat et al. (2017) analyzed the properties of these magnetic helicities in seven parametric simulations of flux emergence (Leake et al. 2013, 2014), during which solar-like active regions are formed, both noneruptive and eruptive. Pariat et al. (2017) observed that the ratio of the current-carrying helicity to the relative helicity was an excellent marker of the eruptive state of the system: only the simulations that would eventually erupt presented high values of that ratio, and only at times before the eruption. Noneruptive simulations, as well as the eruptive simulations after the eruption, displayed low values of the ratio. Zuccarello et al. (2018) further studied this ratio on different numerical experiments (Zuccarello et al. 2015). In four line-tied boundary-driven numerical simulations of solar coronal eruptions (and a noneruptive control case) for which the eruption/instability time was precisely estimated they showed that the eruptions were taking place for the same value of the helicity ratio, within the helicity measurement precision. Other physical

quantities such as magnetic energies did not present the same behavior. They concluded that the eruption process could be related to a threshold in the helicity ratio and that this quantity not only is related to the eruptivity of the system but may also be directly associated with the eruption driver.

From these recent promising results stems the need to better understand the contribution entering into the relative helicity decomposition. This is the goal of the present study, which aims to provide an analytical formulation for the time variation of both the current-carrying helicity and the volume-threading helicity. Only the study of their time variations allows us to ascertain whether these quantities are independently conserved in ideal MHD, in the same way as was done for magnetic helicity.

Additionally, if relative helicity can be studied and tracked from its flux through the photosphere, it is mostly thanks to its conservation property. Can the same be applied to the terms of the relative helicity decomposition? Can the flux of the current-carrying helicity be solely used to study its accumulation in the solar corona? Or are 3D extrapolation and modeling of the solar corona necessary steps to analyze the decomposition of magnetic helicity in solar active regions?

In this paper, we first present the time variation of the terms in the helicity decomposition (see Section 2). Using data from three different simulations of solar-like phenomena (active region formation via flux emergence with or without eruption, and a boundary-driven solar jet), we verify our analytical derivations and study carefully the dynamics of the current-carrying and volume-threading helicities in the different phases of the simulations: magnetic energy buildup and impulsive energy release (see Section 3). In the conclusion (see Section 4), we discuss the impact of the nonconservation of these helicities for their estimations in solar observations.

2. Magnetic Helicity

2.1. Relative Magnetic Helicity

A scalar description of the geometrical properties of magnetic field lines is provided by magnetic helicity, which is defined as follows:

$$H_m = \int_V \mathbf{A} \cdot \mathbf{B} dV = \int_V \mathbf{A} \cdot \nabla \times \mathbf{A} dV, \quad (1)$$

with \mathbf{A} the vector potential of the studied magnetic field, \mathbf{B} , which is prescribed in the fixed volume V bounded by the surface S . This definition is, however, unpractical for the study of most natural plasmas. Indeed, under the gauge transformation, $\mathbf{A}' \rightarrow \mathbf{A} + \nabla\psi$, with ψ an arbitrary function; H_m is invariant if and only if V is a magnetically bounded volume, i.e., if $\mathbf{B} \cdot \mathbf{n}|_S = 0$, \mathbf{n} being the outward-pointing unit vector normal on S . This condition is not satisfied when considering the solar corona, as important magnetic fluxes are threading through the solar photosphere. This led to the introduction of the concept of relative magnetic helicity by Berger & Field (1984), in which a gauge-invariant magnetic helicity is computed introducing a reference field. The most commonly used reference magnetic field is the potential field, \mathbf{B}_p , the unique current-free field having the same distribution of flux \mathbf{B}

through the surface S . It satisfies

$$\begin{cases} \nabla \times \mathbf{B}_p = 0 \\ \mathbf{n} \cdot (\mathbf{B} - \mathbf{B}_p)|_S = 0. \end{cases} \quad (2)$$

The potential field can thus be defined by a scalar function ϕ such as $\nabla\phi = \mathbf{B}_p$. The scalar potential is computed as the solution of the Laplace equation:

$$\begin{cases} \Delta\phi = 0 \\ \frac{\partial\phi}{\partial n}|_S = (\mathbf{n} \cdot \mathbf{B})|_S. \end{cases} \quad (3)$$

The definition of relative magnetic helicity that we use throughout the paper is the one given by Finn & Antonsen (1985):

$$H_v = \int_V (\mathbf{A} + \mathbf{A}_p) \cdot (\mathbf{B} - \mathbf{B}_p) dV. \quad (4)$$

This choice enables H_v to be independently invariant to the gauge transformations of both \mathbf{A} and \mathbf{A}_p . Relative magnetic helicity can be divided into two terms (Berger 2003):

$$H_v = H_j + H_{pj}, \quad (5)$$

$$H_j = \int_V (\mathbf{A} - \mathbf{A}_p) \cdot (\mathbf{B} - \mathbf{B}_p) dV, \quad (6)$$

$$H_{pj} = 2 \int_V \mathbf{A}_p \cdot (\mathbf{B} - \mathbf{B}_p) dV. \quad (7)$$

Considering the nonpotential magnetic field, $\mathbf{B}_j = \mathbf{B} - \mathbf{B}_p$, the vector \mathbf{A}_j , defined as $\mathbf{A}_j = \mathbf{A} - \mathbf{A}_p$, is a vector potential of \mathbf{B}_j since it verifies

$$\begin{aligned} \nabla \times \mathbf{A}_j &= \nabla \times \mathbf{A} - \nabla \times \mathbf{A}_p \\ &= \mathbf{B} - \mathbf{B}_p = \mathbf{B}_j. \end{aligned} \quad (8)$$

Thus, H_j and H_{pj} can be expressed as

$$H_j = \int_V \mathbf{A}_j \cdot \mathbf{B}_j dV, \quad (9)$$

$$H_{pj} = 2 \int_V \mathbf{A}_p \cdot \mathbf{B}_j dV. \quad (10)$$

The term H_j thus corresponds to the classical magnetic helicity (Equation (6)) of the nonpotential magnetic field \mathbf{B}_j , for which S is a flux surface by construction, while H_{pj} can be associated with a volume-threading helicity between \mathbf{B}_p and \mathbf{B}_j . Since the decomposition of \mathbf{B} into \mathbf{B}_p and \mathbf{B}_j is unique, the decomposition of H_v in H_j and H_{pj} is also unique. This decomposition is further relevant since both H_j and H_{pj} are gauge invariant.

Studying the time evolution of the relative magnetic helicity, Pariat et al. (2015) established the following equation:

$$\begin{aligned} \frac{dH_v}{dt} &= \frac{dH_v}{dt} \Big|_{\text{Diss}} + \frac{dH_v}{dt} \Big|_{\text{Bp,var}} \\ &+ F_{Vn} + F_{Bn} + F_{AAp} + F_\phi, \end{aligned} \quad (11)$$

with

$$\frac{dH_v}{dt} \Big|_{\text{Diss}} = -2 \int_V (\mathbf{R} \cdot \mathbf{B}) dV, \quad (12)$$

$$\frac{dH_v}{dt} \Big|_{\text{Bp,var}} = 2 \int_V \frac{\partial\phi}{\partial t} \nabla \cdot \mathbf{A}_p dV, \quad (13)$$

$$F_{Vn} = -2 \int_S (\mathbf{B} \cdot \mathbf{A}) \mathbf{v} \cdot dS, \quad (14)$$

$$F_{Bn} = 2 \int_S (\mathbf{v} \cdot \mathbf{A}) \mathbf{B} \cdot dS, \quad (15)$$

$$F_{AAp} = \int_S (\mathbf{A} - \mathbf{A}_p) \times \frac{\partial}{\partial t} (\mathbf{A} + \mathbf{A}_p) \cdot dS, \quad (16)$$

$$F_\phi = -2 \int_S \frac{\partial\phi}{\partial t} \mathbf{A}_p \cdot dS, \quad (17)$$

where \mathbf{R} is the nonideal MHD contribution to the electric field, such that $\mathbf{E} = -\mathbf{v} \times \mathbf{B} + \mathbf{R}$. Equation (11) assumes that the dynamics follow ideal MHD at the boundary of the domain, i.e., $\mathbf{R}|_S = 0$. Without that hypothesis, one would have a nonideal term such as

$$\begin{aligned} \frac{dH_v}{dt} &= \frac{dH_v}{dt} \Big|_{\text{Non-ideal}} + \frac{dH_v}{dt} \Big|_{\text{Bp,var}} \\ &+ F_{Vn} + F_{Bn} + F_{AAp} + F_\phi, \end{aligned} \quad (18)$$

with

$$\frac{dH_v}{dt} \Big|_{\text{Non-ideal}} = -2 \int_V (\nabla \times \mathbf{R}) \cdot \mathbf{A} dV \quad (19)$$

$$= \frac{dH_v}{dt} \Big|_{\text{Diss}} + F_{\text{Non-ideal}} \quad (20)$$

and

$$F_{\text{Non-ideal}} = -2 \int_S (\mathbf{R} \times \mathbf{A}) \cdot dS. \quad (21)$$

This surface term is usually neglected in observation, but it can be important in specific simulations, where it must then be explicitly calculated. We also note that if the nonideal term of \mathbf{E} derives from a scalar potential, i.e., if there is a function Θ with $\mathbf{R} = \nabla\Theta$, one would have

$$\frac{dH_v}{dt} \Big|_{\text{Non-ideal}} = 0. \quad (22)$$

The helicity time variation (Equation (18)) contains both volume and flux contributions and cannot, in general, be expressed as a function of boundary values alone. In an active solar-like case, Pariat et al. (2015) showed that the dissipation term $dH_v/dt|_{\text{Diss}}$ is very small, even though strong nonideal effects are present. They also stated that imposing the Coulomb gauge on \mathbf{A}_p makes $dH_v/dt|_{\text{Bp,var}}$ null, and hence relative magnetic helicity is a conserved quantity in ideal MHD, i.e., its variations in a volume are only due to flux transfers through the boundaries.

2.2. Time Variations of the Nonpotential Magnetic Helicity

Following Pariat et al. (2015), we aim to determine the time variation of the current-carrying helicity, H_j . Assuming that the volume V is fixed, we differentiate H_j in time:

$$\begin{aligned} \frac{dH_j}{dt} &= \int_V \frac{\partial}{\partial t} \mathbf{A}_j \cdot (\mathbf{B} - \mathbf{B}_p) dV \\ &+ \int_V \mathbf{A}_j \cdot \frac{\partial}{\partial t} (\mathbf{B} - \mathbf{B}_p) dV. \end{aligned} \quad (23)$$

Using the Gauss divergence theorem for the first term and after a combination with the second integral, we find

$$\begin{aligned} \frac{dH_j}{dt} &= 2 \int_V \mathbf{A}_j \cdot \frac{\partial \mathbf{B}}{\partial t} dV - 2 \int_V \mathbf{A}_j \cdot \frac{\partial \mathbf{B}_p}{\partial t} dV \\ &\quad + \int_S \mathbf{A}_j \times \frac{\partial}{\partial t} \mathbf{A}_j \cdot dS. \end{aligned} \quad (24)$$

We choose to keep this form for the flux term and to treat the volume terms separately. We note that only the sum of these terms is properly defined physically, i.e., is gauge invariant: the three terms are not independently gauge invariant. Using the scalar potential ϕ of \mathbf{B}_p and the Gauss divergence theorem, we can decompose the second term of Equation (24):

$$\begin{aligned} -2 \int_V \mathbf{A}_j \cdot \frac{\partial \mathbf{B}_p}{\partial t} dV &= -2 \int_S \frac{\partial \phi}{\partial t} \mathbf{A}_j \cdot dS \\ &\quad + 2 \int_V \frac{\partial \phi}{\partial t} \nabla \cdot \mathbf{A}_j dV. \end{aligned} \quad (25)$$

We then use the Faraday law: $\partial \mathbf{B} / \partial t = -\nabla \times \mathbf{E}$. The first volume term of Equation (24) can be written as

$$\begin{aligned} 2 \int_V \mathbf{A}_j \cdot \frac{\partial \mathbf{B}}{\partial t} dV &= 2 \int_S \mathbf{A}_j \cdot \nabla \times (\mathbf{v} \times \mathbf{B} - \mathbf{R}) dV \\ &= 2 \int_V (\nabla \times (\mathbf{v} \times \mathbf{B})) \cdot \mathbf{A}_j dV \\ &\quad - 2 \int_V (\nabla \times \mathbf{R}) \cdot \mathbf{A}_j dV. \end{aligned} \quad (26)$$

As a last step in the decomposition, we use the Gauss divergence theorem on the ideal term with

$$\begin{aligned} 2 \int_V (\nabla \times (\mathbf{v} \times \mathbf{B})) \cdot \mathbf{A}_j dV &= -2 \int_V ((\mathbf{v} \times \mathbf{B}) \cdot \mathbf{B}_p) dV \\ &\quad - 2 \int_S (\mathbf{B} \cdot \mathbf{A}_j) \mathbf{v} \cdot dS \\ &\quad + 2 \int_S (\mathbf{v} \cdot \mathbf{A}_j) \mathbf{B} \cdot dS. \end{aligned} \quad (27)$$

Finally, the variation of the magnetic helicity of the nonpotential magnetic field can be decomposed as

$$\begin{aligned} \frac{dH_j}{dt} &= \frac{dH_j}{dt} \Big|_{\text{Non-ideal}} + \frac{dH_j}{dt} \Big|_{\text{Bp,var}} + \frac{dH_j}{dt} \Big|_{\text{Transf}} \\ &\quad + F_{Vn,Aj} + F_{Bn,Aj} + F_{Aj,Aj} + F_{\phi,Aj}, \end{aligned} \quad (28)$$

with

$$\frac{dH_j}{dt} \Big|_{\text{Non-ideal}} = -2 \int_V \nabla \times \mathbf{R} \cdot \mathbf{A}_j dV, \quad (29)$$

$$\frac{dH_j}{dt} \Big|_{\text{Transf}} = -2 \int_V (\mathbf{v} \times \mathbf{B}) \cdot \mathbf{B}_p dV, \quad (30)$$

$$\frac{dH_j}{dt} \Big|_{\text{Bp,var}} = 2 \int_V \frac{\partial \phi}{\partial t} \nabla \cdot \mathbf{A}_j dV, \quad (31)$$

$$F_{Vn,Aj} = -2 \int_S (\mathbf{B} \cdot \mathbf{A}_j) \mathbf{v} \cdot dS, \quad (32)$$

$$F_{Bn,Aj} = 2 \int_S (\mathbf{v} \cdot \mathbf{A}_j) \mathbf{B} \cdot dS, \quad (33)$$

$$F_{Aj,Aj} = \int_S \mathbf{A}_j \times \frac{\partial}{\partial t} \mathbf{A}_j \cdot dS, \quad (34)$$

$$F_{\phi,Aj} = -2 \int_S \frac{\partial \phi}{\partial t} \mathbf{A}_j \cdot dS. \quad (35)$$

The decomposition obtained possesses similarities to the time variation of the relative helicity. Apart from $dH_j/dt|_{\text{Transf}}$, all the terms that appear in the time variation of H_j (Equation (28)) have their equivalent in the decomposition of dH/dt (Equation (18)). We find a flux $F_{Vn,Aj}$ related to the normal component of the velocity, v_n , and $F_{Bn,Aj}$ related to the normal component of the field, B_n . The volume term $dH_j/dt|_{\text{Bp,var}}$ related to the time variation of the magnetic field \mathbf{B}_p also appears. The difference with the terms of the time variation of the relative helicity is the dependence on \mathbf{A}_j instead of \mathbf{A} .

Unlike H_v , even in ideal MHD the time variation of H_j contains both volume and flux contributions. The term $dH_j/dt|_{\text{Transf}}$ in Equation (30) is generally not null in ideal MHD (see Section 2.4 for more discussion about this term). Theoretically, H_j is not a conserved quantity of ideal MHD, unlike the classical magnetic helicity H_m and the relative magnetic helicity H_v written in specific gauge conditions.

The majority of terms depend on the difference \mathbf{A}_j between the two vector potentials \mathbf{A} and \mathbf{A}_p . Therefore, by imposing specific relations between these, it is possible to eliminate some of the contributions to the time variation of H_j (see Section 2.5).

Moreover, since the individual terms are not gauge invariant, only their sum has true physical relevance. The intensity of the flux terms depends on the gauge selected.

2.3. Time Variation of the Volume-threading Helicity

Now considering H_{pj} , following similar steps to those for H_j , we can derive the general equation of its time variation:

$$\begin{aligned} \frac{dH_{pj}}{dt} &= \frac{dH_{pj}}{dt} \Big|_{\text{Non-ideal}} + \frac{dH_{pj}}{dt} \Big|_{\text{Bp,var}} + \frac{dH_{pj}}{dt} \Big|_{\text{Transf}} \\ &\quad + F_{Vn,Ap} + F_{Bn,Ap} + F_{Aj,Ap} + F_{\phi,Ap}, \end{aligned} \quad (36)$$

with

$$\frac{dH_{pj}}{dt} \Big|_{\text{Non-ideal}} = -2 \int_V \nabla \times \mathbf{R} \cdot \mathbf{A}_p dV, \quad (37)$$

$$\frac{dH_{pj}}{dt} \Big|_{\text{Transf}} = 2 \int_V (\mathbf{v} \times \mathbf{B}) \cdot \mathbf{B}_p dV, \quad (38)$$

$$\frac{dH_{pj}}{dt} \Big|_{\text{Bp,var}} = 2 \int_V \frac{\partial \phi}{\partial t} \nabla \cdot (\mathbf{A}_p - \mathbf{A}_j) dV, \quad (39)$$

$$F_{Vn,Ap} = -2 \int_S (\mathbf{B} \cdot \mathbf{A}_p) \mathbf{v} \cdot dS, \quad (40)$$

$$F_{Bn,Ap} = 2 \int_S (\mathbf{v} \cdot \mathbf{A}_p) \mathbf{B} \cdot dS, \quad (41)$$

$$F_{Aj,Ap} = 2 \int_S \mathbf{A}_j \times \frac{\partial}{\partial t} \mathbf{A}_p \cdot dS, \quad (42)$$

$$F_{\phi,Ap} = -2 \int_S \frac{\partial \phi}{\partial t} (\mathbf{A}_p - \mathbf{A}_j) \cdot dS. \quad (43)$$

As with H_j , the time variation of H_{pj} cannot be expressed solely through boundary fluxes, and thus H_{pj} is not a conserved quantity even in ideal MHD when $\mathbf{R} = 0$, unlike H_v , and this is due to the transfer term of Equation (38).

2.4. Helicity Exchange

2.4.1. Helicity Exchange between H_j and H_{pj}

As expected, by summing the time variations of the nonpotential and the volume-threading magnetic helicities (Equations (28) and (36)), we obtain the time variation of the relative magnetic helicity (Equation (18)):

$$\frac{dH_v}{dt} = \frac{dH_j}{dt} + \frac{dH_{pj}}{dt}. \quad (44)$$

Each term in Equation (18) has indeed its counterpart in the decomposition of H_j and H_{pj} , e.g., the sum of $F_{Vn,Ap}$ and $F_{Vn,Aj}$ gives F_{Vn} .

However, the time variations of H_{pj} and H_j each possess a volume contribution that is not present in dH_v/dt . These terms, $dH_x/dt|_{\text{Transf}}$, with x being either j or pj , allow the transfer of helicity between H_{pj} and H_j . They correspond to oppositely signed quantities, i.e.,

$$\left. \frac{dH_j}{dt} \right|_{\text{Transf}} = - \left. \frac{dH_{pj}}{dt} \right|_{\text{Transf}}. \quad (45)$$

The helicity transfer term is a volume quantity that allows the transformation of one form of helicity into the other. This transformation occurs within the full domain of study. Our analysis of several numerical experiments (see Section 3) shows that this quantity actually reaches high values compared to the other terms and can dominate the evolution of both H_j and H_{pj} .

It is thus essential to have a precise understanding of the term $dH_j/dt|_{\text{Transf}}$. A study of this term permits us to quantify the exchange between the helicities H_j and H_{pj} in the volume, an exchange that does not affect the relative helicity, H_v . It is particularly worth noting that $dH_j/dt|_{\text{Transf}}$ is a gauge-invariant quantity. It indeed only depends on \mathbf{v} , \mathbf{B} , and \mathbf{B}_p and does not have any vector potential contribution.

There are several possible decompositions for $dH_j/dt|_{\text{Transf}}$. However, despite several different attempts, we could not find a way to express this term solely as a flux contribution, i.e., as an integral on the boundary. For example, we can write

$$\begin{aligned} -2 \int_V (\mathbf{v} \times \mathbf{B}) \cdot \mathbf{B}_p dV &= -2 \int_V ((\mathbf{v} \times \mathbf{B}) \cdot \nabla \phi) dV \\ &= -2 \int_S \phi (\mathbf{v} \times \mathbf{B}) \cdot d\mathbf{S} \\ &\quad + 2 \int_V \phi \nabla \cdot (\mathbf{v} \times \mathbf{B}) dV. \end{aligned} \quad (46)$$

A volume integral contribution remains, however. We have numerically tested this decomposition (in a similar manner to that performed in Section 3) and concluded that it presents no advantage over its $(\mathbf{v} \times \mathbf{B}) \cdot \mathbf{B}_p$ form.

2.4.2. Helicity Exchange with the Surrounding Environment

In the specific case of the resistive MHD, the nonideal contribution to the electric field can be explicitly written as $\mathbf{R} = \eta \nabla \times \mathbf{B}$, with η corresponding to the magnetic resistivity. Using the Gauss-divergence theorem, the nonideal term in Equation (28) can be decomposed into a surface term and a

dissipation term:

$$\left. \frac{dH_j}{dt} \right|_{\text{Non-ideal}} = -2 \int_V \nabla \times (\eta \nabla \times \mathbf{B}) \cdot \mathbf{A}_j dV \quad (47)$$

$$= \left. \frac{dH_j}{dt} \right|_{\text{Diss}} + F_{\text{Non-ideal,Aj}}, \quad (48)$$

with

$$\left. \frac{dH_j}{dt} \right|_{\text{Diss}} = -2 \int_V \eta (\nabla \times \mathbf{B}) \cdot \mathbf{B}_j dV, \quad (49)$$

$$F_{\text{Non-ideal,Aj}} = -2 \int_S \eta (\nabla \times \mathbf{B}) \times \mathbf{A}_j \cdot d\mathbf{S}. \quad (50)$$

The dissipation term, $dH_j/dt|_{\text{Diss}}$, as well as the transfer term, $dH_j/dt|_{\text{Transf}}$, is gauge invariant. By defining $dH_j/dt|_{\text{Own}}$ as

$$\begin{aligned} \left. \frac{dH_j}{dt} \right|_{\text{Own}} &= \left. \frac{dH_j}{dt} \right|_{\text{Bp,var}} + F_{\text{Non-ideal,Aj}} \\ &\quad + F_{\phi,Aj} + F_{Vn,Aj} + F_{Bn,Aj} + F_{Aj,Aj}, \end{aligned} \quad (51)$$

we obtain an equation for the time variation of H_j that is formed solely of gauge-invariant terms:

$$\frac{dH_j}{dt} = \left. \frac{dH_j}{dt} \right|_{\text{Own}} + \left. \frac{dH_j}{dt} \right|_{\text{Diss}} + \left. \frac{dH_j}{dt} \right|_{\text{Transf}}. \quad (52)$$

Similarly, we can construct a time variation of H_{pj} with gauge-invariant terms only:

$$\frac{dH_{pj}}{dt} = \left. \frac{dH_{pj}}{dt} \right|_{\text{Own}} + \left. \frac{dH_{pj}}{dt} \right|_{\text{Diss}} - \left. \frac{dH_j}{dt} \right|_{\text{Transf}}, \quad (53)$$

with

$$\left. \frac{dH_{pj}}{dt} \right|_{\text{Diss}} = -2 \int_V \eta (\nabla \times \mathbf{B}) \cdot \mathbf{B}_p dV, \quad (54)$$

$$\begin{aligned} \left. \frac{dH_{pj}}{dt} \right|_{\text{Own}} &= \left. \frac{dH_{pj}}{dt} \right|_{\text{Bp,var}} + F_{\text{Non-ideal,Ap}} \\ &\quad + F_{Vn,Ap} + F_{Bn,Ap} + F_{Aj,Ap} + F_{\phi,Ap}, \end{aligned} \quad (55)$$

and

$$F_{\text{Non-ideal,Aj}} = -2 \int_S \eta (\nabla \times \mathbf{B}) \times \mathbf{A}_p \cdot d\mathbf{S}. \quad (56)$$

The ‘‘Own’’ terms correspond to the proper helicity variation of either H_j or H_{pj} . They do not, strictly speaking, correspond to a flux through the boundary since a volume contribution is also present for both H_j and H_{pj} : $dH_x/dt|_{\text{Bp,var}}$. These volume contributions are, however, gauge dependent. A particular choice of gauges (the Coulomb gauge for \mathbf{A} and \mathbf{A}_p) can nonetheless make them null. Written with this choice of gauges, $dH_j/dt|_{\text{Own}}$ and $dH_{pj}/dt|_{\text{Own}}$ then only appear as pure boundary flux contributions, which would correspond to a transfer of helicities between the studied domain and its surrounding environment. Like $dH_j/dt|_{\text{Transf}}$, both ‘‘Own’’ terms are independently gauge-invariant quantities. Equations (52) and (53) thus only involve independently gauge-invariant terms. Their analysis is thus of particular interest, as will be shown in our study of the helicity evolution in different numerical experiments (see Section 3).

2.5. Specific Gauge Conditions

While the variation of H_j and H_{pj} can be generally described by Equations (6) and (7) for any gauge, the choice of some specific additional constraints on the gauge allows us to simplify the expression of their time variations and possibly their computation.

A first possible additional constraint is to use the Coulomb gauge for the vector potential of the potential field, \mathbf{A}_p , i.e.,

$$\nabla \cdot \mathbf{A}_p = 0. \quad (57)$$

In this gauge, the volume contributions related to the variation of the potential field become

$$\left. \frac{dH_{pj}}{dt} \right|_{\text{Bp,var,cond (57)}} = - \left. \frac{dH_j}{dt} \right|_{\text{Bp,var,cond (57)}} \quad (58)$$

$$= -2 \int_V \frac{\partial \phi}{\partial t} \nabla \cdot \mathbf{A} dV. \quad (59)$$

While condition (57) leads to a cancellation of $dH_v/dt|_{\text{Bp,var}}$ for the relative helicity (e.g., Pariat et al. 2015), this is not the case for the evolution of its components H_j and H_{pj} .

Another possible additional constraint that can be imposed is to link the vector potentials \mathbf{A} and \mathbf{A}_p on the boundary, i.e.,

$$\mathbf{A}|_S - \mathbf{A}_p|_S = \mathbf{A}_j|_S = 0. \quad (60)$$

This condition ensures the nullity of $F_{\mathbf{A}\mathbf{A}_p,\mathbf{A}_p}$ and all the fluxes of the form F_{α,\mathbf{A}_j} (with $\alpha \in \{\mathbf{V}_n, \mathbf{B}_n, \mathbf{A}_j, \phi, \text{Nonideal}\}$) in Equation (51). Under such a condition, the time variation of the nonpotential magnetic helicity can be described only as a volume variation, consisting of the sum of the transfer term, $dH_j/dt|_{\text{Transf}}$, and the term $dH_j/dt|_{\text{Bp,var}}$. There is no contribution of helicity due to any fluxes through the boundary.

Another possible constraint is to eliminate the normal component of \mathbf{A}_p on the boundary:

$$\mathbf{A}_p \cdot \mathbf{n}|_S = 0. \quad (61)$$

This choice, combined with the previous one in Equation (60), leads to the elimination of the term F_{ϕ,\mathbf{A}_p} .

Combining these conditions and assuming that the evolution follows the ideal MHD evolution, i.e., supposing

$$\begin{cases} \mathbf{R} = 0 \\ \nabla \cdot \mathbf{A}_p = 0 \\ \mathbf{A}_p \cdot \mathbf{n}|_S = 0 \\ \mathbf{A}|_S - \mathbf{A}_p|_S = 0 \end{cases} \quad (62)$$

as is frequently assumed when studying the flux of relative magnetic helicity (e.g., Démoulin & Pariat 2009), we obtain the following form of the time variations of H_j and H_{pj} :

$$\left. \frac{dH_j}{dt} \right|_{\text{cond. (62)}} = 2 \int_V \frac{\partial \phi}{\partial t} \nabla \cdot \mathbf{A} dV - 2 \int_V (\mathbf{v} \times \mathbf{B}) \cdot \mathbf{B}_p dV \quad (63)$$

and

$$\begin{aligned} \left. \frac{dH_{pj}}{dt} \right|_{\text{cond. (62)}} &= 2 \int_V (\mathbf{v} \times \mathbf{B}) \cdot \mathbf{B}_p dV - 2 \int_V \frac{\partial \phi}{\partial t} \nabla \cdot \mathbf{A} dV \\ &+ 2 \int_S ((\mathbf{v} \cdot \mathbf{A}_p)\mathbf{B} - (\mathbf{B} \cdot \mathbf{A}_p)\mathbf{v}) \cdot d\mathbf{S}. \end{aligned} \quad (64)$$

With these specific conditions H_j does not exchange with the outside environment (no surface fluxes). The flux of the total relative helicity, H_v , is uniquely due to the flux of H_{pj} through the boundaries. H_{pj} can additionally undergo variations in the volume. These volume variations are actually helicity exchanges with H_j (see Equations (30) and (38)). The time evolution of H_j is indeed only related to volume conversion from H_{pj} .

While condition (62) appears particularly strong, it is de facto a usual assumption in observational methods analyzing the flux of helicity through the solar photosphere. Our analysis highlights the internal exchange in the volume between the two helicities. It indicates that the traditional helicity flux method cannot be used to evaluate the current-carrying component, H_j , in observations. This point will be further highlighted in our analysis of numerical simulations of the dynamics of the solar corona (see the following section) and in the conclusion (see Section 4).

3. Numerical Tests

In order to quantify the transfer of helicity and to numerically validate the time variations of the two helicities (see Equations (28) and (36)), we analyze the magnetic field of three different numerical simulations produced by two different 3D MHD codes.

3.1. Test Cases

3.1.1. Jet Simulation

The first test case is a 3D MHD numerical simulation of the generation of a solar coronal jet (Pariat et al. 2009). The initial magnetic field in this numerical experiment is formed by a 3D null point (see Figure 1). The volume contains two different magnetic connectivity domains: open and closed. The simulation lasts between $t = 0$ and $t = 1600$ in the system's nondimensional units. In the pre-eruptive phase $t \in [0, 920]$, the energy and the helicity are accumulated by line-tied twisting motions of the central magnetic polarity. These motions preserve the distribution of the vertical magnetic field component, B_z , at the bottom boundary. Thanks to topological constraints, magnetic reconnection is inhibited during that phase (see discussion in Section 2 of Pariat et al. 2009), and the dynamics of the system can thus be considered quasi-ideal MHD before $t \sim 920$.

At around $t \sim 920$, magnetic reconnection between closed and open field lines induces the formation of a jet. The period after $t \sim 920$ is designated as the nonideal phase, in opposition to the pre-jet phase. During this nonideal MHD evolution, with intense magnetic reconnection, free magnetic energy is dissipated and released by the jet. The helicity is transferred outside through the domain boundaries by a nonlinear Alfvénic wave constituting the jet (see Pariat et al. 2016, for the physics of the driving mechanism of the jet). The jet lasts between $t \sim 920$ and $t \sim 1200$. After $t \sim 1200$, the jet plasma has left

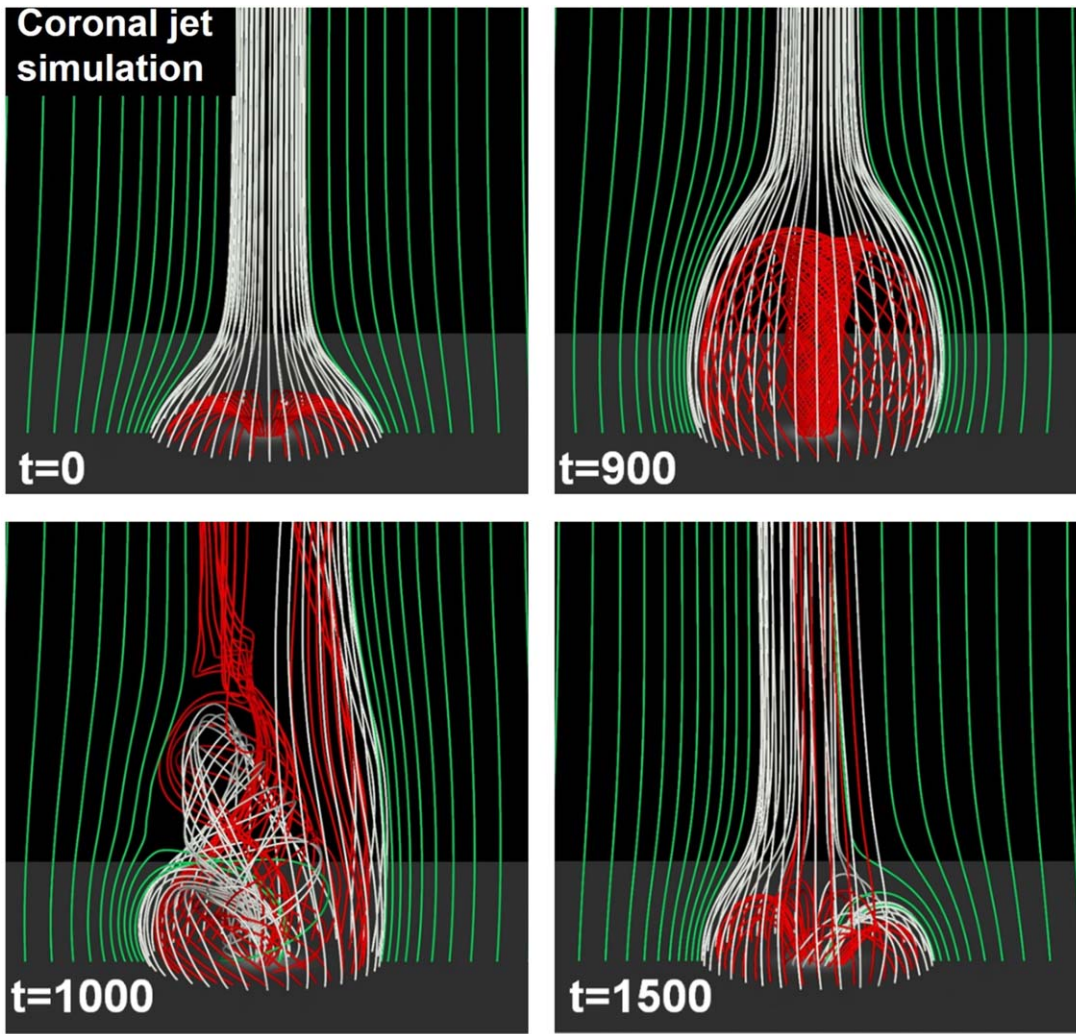


Figure 1. Snapshots of the magnetic field evolution during the generation of a coronal jet. The red field lines are initially closed. The green and white field lines are initially open. At $t = 900$ the system is in its pre-eruption stage. At $t = 1000$ the system is erupting. Helicity is ejected upward along newly opened reconnected field lines. At $t = 1500$ the system is slowly relaxing to its final stage.

the domain and no high-velocity upflows are present in the studied domain. The system slowly relaxes toward its initial potential state, thanks to low-intensity reconnections. A low-amplitude, large-scale standing wave remains in the domain (Pariat et al. 2015). At the end of the simulation, very few twisted field lines remain.

Physical quantities are outputted with a cadence of $\Delta t = 50$ for $t \in [0, 700]$ and $\Delta t = 10$ for $t \in [700, 1600]$, the higher cadence allowing a better analysis of the nonideal phase. The output data grid corresponds to a sample of the simulation computation grid. The volume analyzed in the present study is a 3D mesh of 129^3 points, whose range is $x \in [-6, 6]$, $y \in [-6, 6]$, and $z \in [0, 12]$, hence corresponding to the central domain of the simulation of Pariat et al. (2009). The data used for the present analysis correspond to the full 3D velocity and magnetic vector fields.

The magnetic field presents a finite level of nonsolenoidality ($\Delta \cdot \mathbf{B} \neq 0$), unavoidably induced by the discretized data set, that limits the precision of the helicity computation (see Section 7 of Valori et al. 2016). To quantify the impact of this effect, following Valori et al. (2016), we determine the nonsolenoidal energy E_{ns} introduced by Valori et al. (2013). This energy corresponds to the sum of artifact additional contributions, due

to finite nonsolenoidality of \mathbf{B} , to the Thompson decomposition of energy. As mentioned in Pariat et al. (2015), the ratio E_{ns}/E of the nonsolenoidal energy to the total magnetic energy is lower than 0.1%: it highlights the excellent solenoidality of the magnetic field data. Since the nonsolenoidality is the largest source of errors in helicity calculation (Valori et al. 2016), such a small value supports the excellent precision on the helicity computation.

3.1.2. Flux Emergence Simulations

The next two tests employed in our study are based on the 3D visco-resistive MHD numerical experiments of Leake et al. (2013, 2014). The two simulations considered here present the emergence of the same twisted magnetic flux rope from the upper convection zone into the stratified solar atmosphere (see Figure 2). In the coronal domain, a constant value for the resistivity is assumed, $\eta = 0.01$. These simulations have also been analyzed by Valori et al. (2016), Guennou et al. (2017), and Pariat et al. (2017).

For our present analysis, the flux rope emerges at the bottom boundary, the minimum temperature region emulating the solar photosphere, and forms a solar-like bipolar active region. The

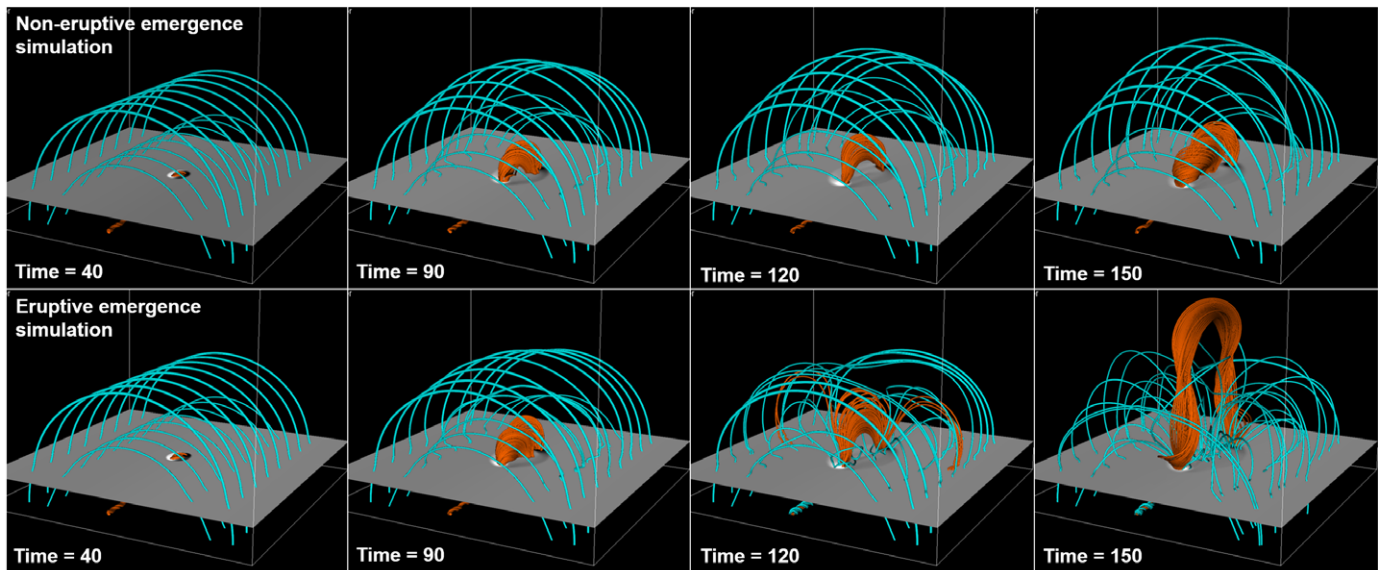


Figure 2. Snapshots comparing the evolution of the magnetic field in the eruptive (bottom row) and noneruptive (top row) flux emergence simulations. The orange (cyan) field lines initially belong to the emerging flux rope (arcade). The grayscale 2D surface displays the distribution of the magnetic field at the simulated photospheric level. Only the coronal domain, above that boundary, is considered in the present study.

simulations last between $t = 0$ and $t = 200$ in the nondimensional units of the system (see Leake et al. 2013, for more details). The flux rope pierces through the photospheric boundary at $t = 30$. Before that time, the flux rope is moving through the convection zone, a domain not considered in our study.

The same initial twisted magnetic flux rope emerges into a potential coronal field presenting an arcade structure of different intensity and orientation. In Leake et al. (2013) the magnetic arcade is parallel with the top magnetic field of the emerging flux rope. In this setup, the emerging flux rope remains contained within the coronal domain and stabilizes itself. No impulsive ejection of magnetic structure is observed. In the present paper, we analyze the particular simulation obtained with a medium intensity field arcade (MD case in Leake et al. 2013), and we designate it as “noneruptive emergence” throughout this paper.⁴

The second flux emergence simulation that we analyze has an opposite direction of the arcade field compared to the first simulation (MD case in Leake et al. 2014). We refer to this simulation as “eruptive emergence.”⁵ In this geometry, magnetic reconnections between the emerging flux rope and the surrounding arcade field are favored. The emergence of the flux rope eventually induces an eruption: a secondary flux rope is formed, following the emergence, that eventually becomes unstable and is impulsively ejected upward toward the top boundary. The eruption develops between $t \sim 120$ and $t \sim 150$, a period during which the axis of the flux rope presents a high upward velocity before eventually leaving the numerical domain. During the post-eruptive phase, the system relaxes toward a stable configuration.

The original simulations are performed on a 3D irregular Cartesian mesh. Only the coronal domain of the magnetic and velocity field data is extracted and is remapped onto a 3D uniform Cartesian grid using trilinear interpolation. The analyzed-volume range is $x \in [-100, 100]$, $y \in [-100, 100]$,

and $z \in [0.36, 150]$ in the nondimensional units of Leake et al. (2013, 2014). While the domain analyzed is the same as in Valori et al. (2016) and Pariat et al. (2017), the interpolation is performed on a grid with a higher resolution. The number of pixels is 1.5 times larger in each direction compared to the previous helicity analyses. The grid is composed of 311 mesh points along both the horizontal directions, x and y , and 232 along the vertical direction, z .

As with the jet simulation, the divergence of \mathbf{B} is not exactly null, and the energy decomposition presents a finite value of E_{ns} . The value of the ratio E_{ns}/E is lower than 1.5% once the flux rope starts to emerge. Thus, the level of nonsolenoidality remains low, ensuring a good reliability in our calculation of the helicity, as follows from the tests performed in Valori et al. (2016).

3.2. Volume Helicity Estimation

The output of the different simulations are datacubes, on a uniform cuboid Cartesian grid, of the magnetic field \mathbf{B} , the plasma-velocity field \mathbf{v} , and the plasma thermodynamical quantities (not used here). From the 3D magnetic field, the different magnetic helicities, H_v , H_j , and H_{pj} , can be directly computed at each time step.

In the present study, we adopt the method of Valori et al. (2012): at each time step of the simulations, from $\mathbf{B}(t)$ we compute its respective potential magnetic field, $\mathbf{B}_p(t)$, from its scalar potential, $\phi(t)$, which is obtained from a numerical solution of the Laplace Equation (3).

Then, the respective potential vectors $\mathbf{A}(t)$ and $\mathbf{A}_p(t)$ can be computed with a few 1D integrations (see Equation (14) of Valori et al. 2012). This method assumes that the potential vectors satisfy the DeVore gauge (DeVore 2000), in which their vertical component is null at every instant and every point in the domain, i.e.,

$$A_z(x, y, z, t) = A_{p,z}(x, y, z, t) = 0. \quad (65)$$

This condition does not uniquely define the vector potential. Following Pariat et al. (2015, 2017) for the jet and the

⁴ This simulation was denoted “No Erupt MD” in Pariat et al. (2017).

⁵ It was denoted “Erupt MD” in Pariat et al. (2017).

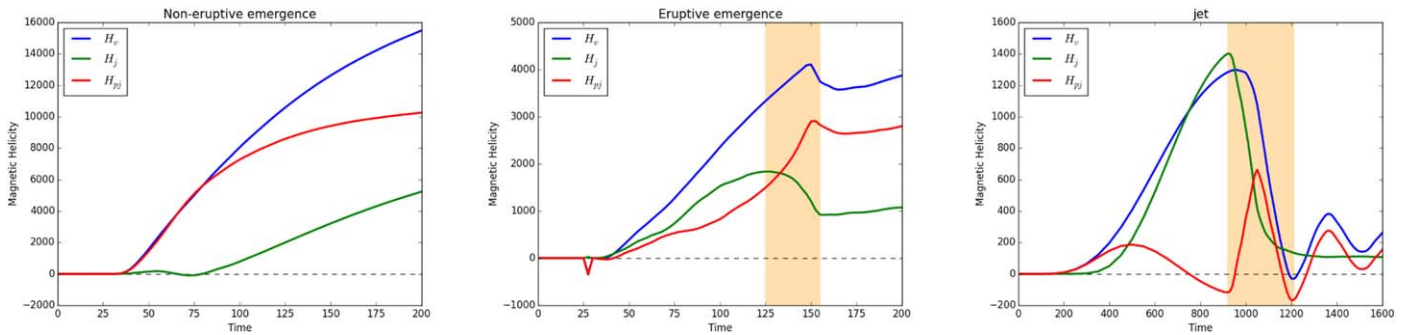


Figure 3. Time evolution of the different magnetic helicities: the relative magnetic helicity (blue lines; Equation (4)), the volume-threading helicity (red lines; Equation (7)) and the nonpotential magnetic helicity (green lines; Equation (6)), for the different simulations studied: from left to right, the nonruptive emergence simulation, the eruptive emergence, and the simulation of the generation of a solar coronal jet. For the eruptive emergence and the jet simulations the yellow vertical band corresponds to the eruptive phases.

emerging flux simulations, respectively, our numerical computation of A_p enforces the Coulomb gauge ($\nabla \cdot A_p = 0$). Following Pariat et al. (2015), this gauge choice is referred to as the DeVore–Coulomb gauge. Additionally, the 1D integration starts at the top boundary of the domain (at height z_{top}), where we enforce the relation

$$A(x, y, z = z_{\text{top}}, t)_{\perp} = A_p(x, y, z = z_{\text{top}}, t)_{\perp}. \quad (66)$$

Finally, the helicities are obtained from this volume integration method using Equations (4), (6), and (7). As mentioned earlier, the resulting helicity shows a residual gauge dependence due to the finite level of solenoidality of \mathbf{B} unavoidably induced by the discretized data set. In our simulations, the errors introduced are minimal and do not affect the helicity estimations, thanks to the low value of E_{ns} (see Section 3).

In Figure 3, we plot the time evolution of the three helicities of our study for the different simulations. We note that for the nonruptive flux emergence simulation, the relative helicity of the system is dominated by the H_{pj} component. For the eruptive flux emergence simulation, the helicity is dominated by H_j before the onset of the eruption (before $t \sim 120$), and then by H_{pj} once the system is relaxing after the eruption. This property has been studied in Pariat et al. (2017) and Zuccarello et al. (2018), who showed that the ratio H_j/H_v was a very good marker of the eruptivity of these simulations.

We observe for the jet simulation that while in the very beginning of the energizing the relative helicity is mostly constituted by H_{pj} (for $t < 400$), the system becomes dominated by H_j between $t \sim 400$ and $t \sim 900$, up until the onset of the jet. After the jet formation, H_j decreases substantially and the system is on average dominated by H_{pj} . This simulation thus seems to confirm the results of Pariat et al. (2017) and Zuccarello et al. (2018); the ratio H_j/H_v appears closely related to the eruptivity in the system; this ratio is low at the start of the energizing, where the system is departing from a potential configuration, becomes high before the onset of the eruptive behavior, and drops to a low value after the eruption, when the system relaxes to a stable state.

3.3. Time Variation Estimations

One goal of the present study is to verify numerically our analytical derivation of the time variations of the nonpotential and volume-threading helicities (Equations (6) and (7)). From three successive outputs of the studied MHD system,

corresponding to three instants separated by a time interval Δt , we directly compute their helicity variation rate for the instant t :

$$\frac{\Delta H_x(t)}{\Delta t} = \frac{H_x(t + \Delta t) - H_x(t - \Delta t)}{2\Delta t}, \quad (67)$$

with x standing for either j or pj .

Along with the estimation of the helicities in the volume and their time differentiation ($\Delta H_j/\Delta t$ and $\Delta H_{pj}/\Delta t$; see Section 3.2), we also evaluate their instantaneous time variation, dH_j/dt and dH_{pj}/dt from Equations (28) and (36).

Our analysis is performed within the resistive MHD paradigm. Besides the resistive term, any other nonideal contributions are not treated by the numerical solvers in the simulations. For our numerical computation of the helicity variations terms, the nonideal effects are thus limited to the inclusion of the dissipation term in Equations (49), (54), (50), and (56).

In the particular case of the jet simulation, the ideal MHD equations are solved, and the resistivity, η , is not specified. Pariat et al. (2015) demonstrated that the helicity dissipation is extremely low for that simulation. Consequently, in the following, for the jet simulation we assume that $\eta = 0$.

The estimation of the latter quantities requires, in addition to the 3D magnetic field, \mathbf{B} , the knowledge of the velocity field, \mathbf{v} , at the boundary of the domain. Moreover, using the magnetic field, the potential magnetic field and the vector potentials are obtained from the volume estimation procedure (see Section 3.2). The different terms that appear in the instantaneous time variation (Equations (28) and (36)) are estimated independently, even though, as already noted in Section 2.4, most of them are not independently gauge invariant. For the quantities that correspond to fluxes, the determination of the surface integrals is calculated systematically as the sum of the contributions from the six boundaries.

It should be noted that for the emergence simulations, for $t \in [25, 30]$, when the top of the flux rope starts to pierce through the photospheric-like layer, the bottom boundary of the data set we analyze, some quantities involve small values, which introduce numerical errors in our helicity estimations. For example, this can be observed in Figure 3(c) as a small peak in the evolution of H_{pj} at $t = 27$ for the eruptive emergence. This numerical artifact leads to fluctuations in the estimation of most terms of the instantaneous time variation, even though the helicities have very small values. To correct

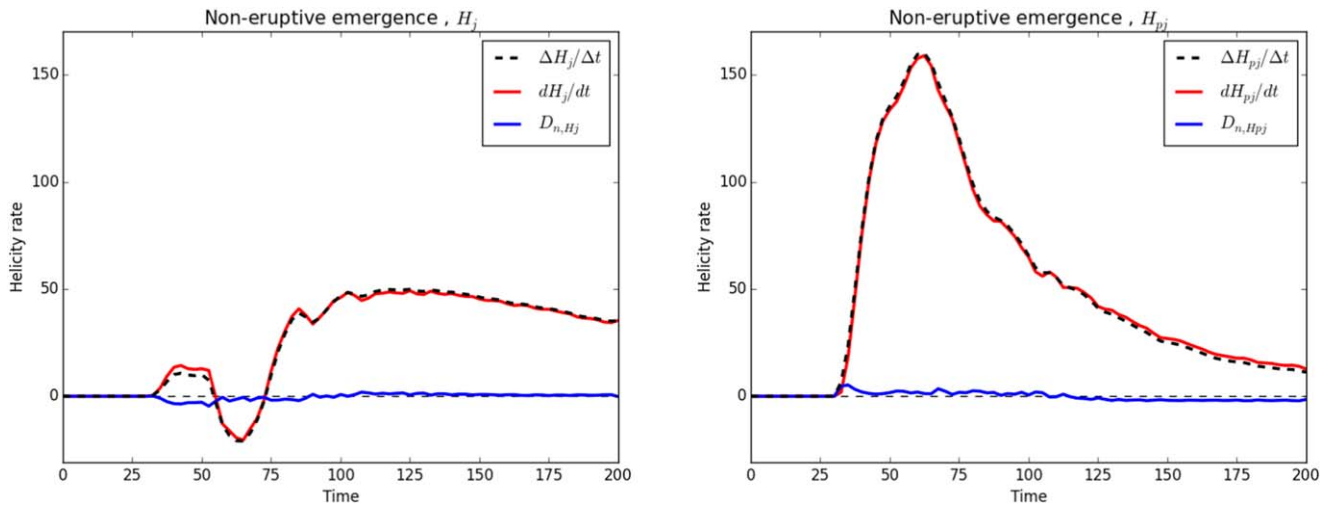


Figure 4. Time evolution of the helicity variation rates, $\Delta H_j/\Delta t$ and $\Delta H_{pj}/\Delta t$ (dashed black curves; Equation (67)), the instantaneous time variations, dH_j/dt and dH_{pj}/dt (solid red curves; Equations (28) and (36)), and the differences of these quantities, D_{n,H_j} and $D_{n,H_{pj}}$ (solid blue curves; Equation (68)), for the noneruptive flux emergence. The left and right panels present the evolution of the nonpotential helicity, H_j , and volume-threading helicity, H_{pj} , respectively.

this problem, we thus set all helicity terms equal to zero for $t < 27$.

3.4. Numerical Validation

In order to validate the analytical derivation of the time variation of the terms in the helicity decomposition (Equations (28) and (36)), we will compare the estimation of the time derivative of the helicity rates obtained from the volume integration method ($\Delta H_j/\Delta t$ and $\Delta H_{pj}/\Delta t$; Equation (67)) with the estimation of the instantaneous time variation (dH_j/dt and dH_{pj}/dt ; Equations (28) and (36)), as discussed in Section 3.3.

Since the numerical evaluation of both the instantaneous time variation of a quantity and its time differentiation involves many operations, some numerical errors are always expected when comparing them. Studying the evolution of relative magnetic helicity, Pariat et al. (2015) found that for the jet simulation, during the quasi-ideal phase, before the onset of the jet, a relative error of about 0.001 exists between the instantaneous rate and the differentiation of the volume quantity. Here, although using different routines, we obtain the same result for H_v as Pariat et al. (2015). This previous test suggests that both results are numerically correct and that these routines can be used for the calculation of the terms in our analytical time variations of H_j and H_{pj} (Equations (28) and (36)).

As noted in the previous section, since the simulations are de facto solving the resistive MHD equation, the additional nonideal contributions are not considered with this paradigm. In order to numerically validate our analytical formula and quantify the correspondence between the left- and right-hand terms of Equations (28) and (36), we evaluate the differences:

$$D_{n,x} = \frac{\Delta H_x}{\Delta t} - \frac{dH_x}{dt} \quad (68)$$

where x corresponds to either j or pj .

Figures 4–6 present the evolution of the time derivative of the volume helicities, the instantaneous variation rate, and their difference. In Figure 6 we note that during the quasi-ideal phase, before the onset of the jet, $D_{n,x}$ remains extremely small, similarly to what has been obtained for the relative helicity H_v .

The mean ratio of $|D_{n,j}|$ to $|dH_j/dt|$ is lower than 3%, and less than 7% for the ratio of $|D_{n,pj}|$ to $|dH_{pj}/dt|$ during that phase. Dissipation being null in ideal MHD, this very low value is coherent with the theory and shows that numerical errors are also very low. The low values of $|D_{n,x}|$ confirm the validity of Equations (28) and (36) about the helicity time variations, which constitute the central result of this study.

During the nonideal phase of the jet simulation, strong nonideal effects are present with intense magnetic reconnections. While the D_n differences present larger values than during the quasi-ideal phase, mostly through the form of fluctuating peaks, their intensity is very weak in comparison with the values of dH_x/dt . During the eruption phase, the mean ratio of $|D_{n,j}|$ to $|dH_j/dt|$ is also about 12%, and 6% for that ratio of $|D_{n,pj}|$ to $|dH_{pj}/dt|$. Equations (28) and (36) are thus valid to a very high degree of accuracy.

As mentioned in Section 3.3, for the flux emergence simulations, we are able to calculate nonideal effects related to the resistivity. Thus, $D_{n,x}$, presented in Figures 4 and 5 for the eruptive and the noneruptive simulations, respectively, is almost entirely associated with numerical errors.

The difference between $\Delta H_x/\Delta t$ and dH_x/dt remains relatively low with respect to the values reached by these quantities. There is an exception, however, during the very initial phase of the flux emergence, for both the eruptive and noneruptive cases, during which the curves of $\Delta H_j/\Delta t$ appear distinct from the ones of dH_j/dt . For $t \in [25, 60]$, we note a high value of $D_{n,j}$ for H_j . This effect is more particularly pronounced for the time variation of H_j . During this period, the mean ratio of $|D_{n,j}|$ to $|dH_j/dt|$ is 14% for both simulations.

We hypothesize that this value of $D_{n,x}$ during that period is due to a temporal undersampling due to relatively low-cadence data available. This phase indeed corresponds to the moment when the flux rope emerges into the coronal domain though the model photosphere, when the bottom boundary in our calculation thus exhibits relatively fast changes.

Neglecting this initial phase, one observes that the values of $D_{n,x}$ remain overall significantly smaller than the values of dH_x/dt . The mean ratios of $|D_{n,j}|$ to $|dH_j/dt|$ and $|D_{n,pj}|$ to $|dH_{pj}/dt|$ are lower than 9% for the eruptive emergence and lower than 5% for the noneruptive simulation.

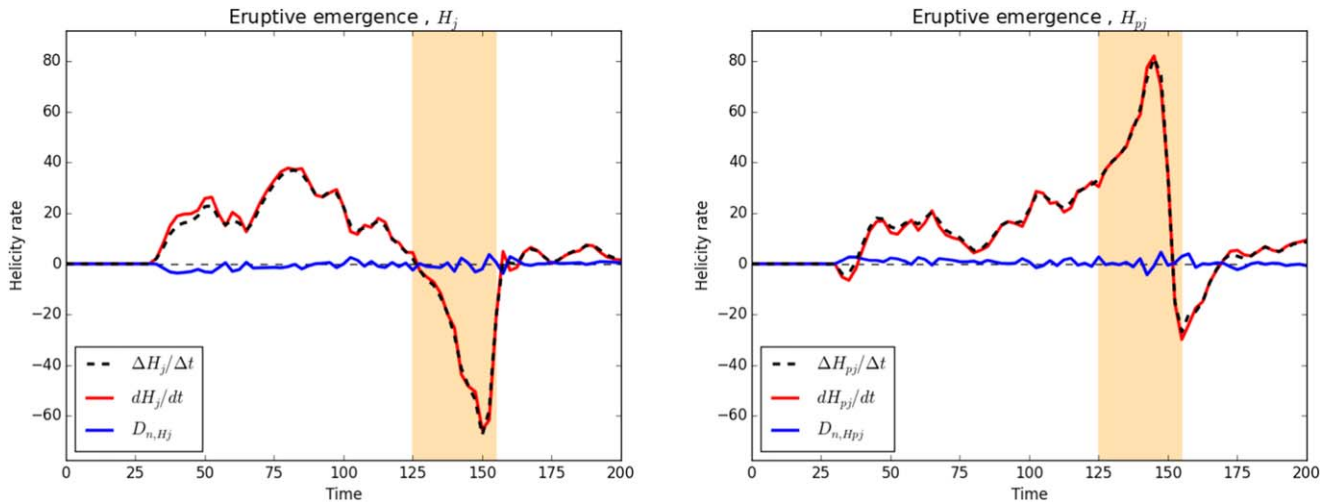


Figure 5. Same as Figure 4, but for the eruptive flux emergence simulation. The yellow bands correspond to the eruptive phase.

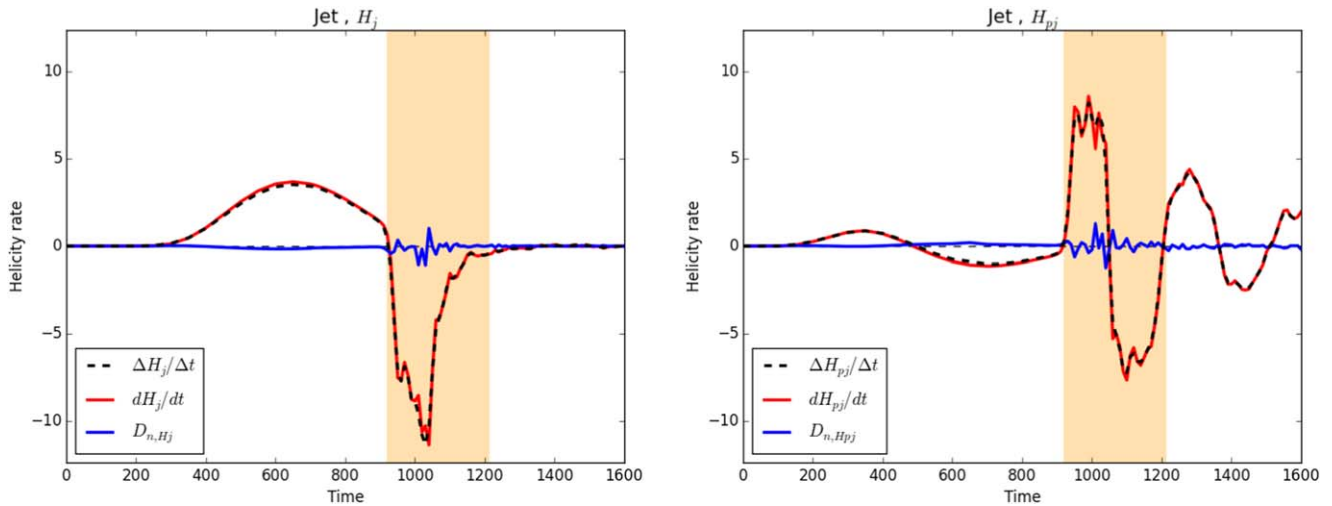


Figure 6. Same as Figure 4, but for the coronal jet simulation. The yellow bands correspond to the eruptive phase.

From the analysis of these three numerical simulations, we conclude that our estimation of dH_x/dt enables a consistent evaluation of the helicity and that Equations (28) and (36) for the time variation of H_j and H_{pj} are satisfactorily numerically verified.

3.5. Helicity Fluxes

In Figures 7 and 8, we compare the different terms that compose the instantaneous time variation of H_j (Equation (28)) and H_{pj} (Equation (36)), respectively. As described in Section 2.4, only the transfer term, the dissipation term, and the sum of the fluxes, $dH_x/dt|_{\text{own}}$, are gauge invariant. The fluxes, $F_{\alpha, \text{Ap}}$ and $F_{\alpha, \text{Aj}}$ (with $\alpha \in \{\text{Vn}, \text{Bn}, \text{Aj}, \phi, \text{Nonideal}\}$), are gauge dependent. Therefore, computed with different gauges, the curves in Figures 7 and 8 might be noticeably different, e.g., as shown in the Appendix. As the individual terms nonetheless inform on the dynamics of the helicity variations within the adopted gauge, we briefly present their evolution here.

In Figures 7 and 8, $dH_x/dt|_{\text{Transf}}$, which is a volume contribution, is not small compared to the other fluxes. It

confirms that H_{pj} and H_j are not conserved quantities. In other words, their time variations cannot be written as only the sum of surface contributions. We also see in Figure 7 that for the three simulations the curves of $\Delta H_j/\Delta t$ are frequently overlaid by $dH_j/dt|_{\text{Transf}}$. The transfer term seems to be essential to understand the evolution of helicities, in particular, for the jet simulation (see Figure 7, right panel), where the other terms are negligible compared to $dH_j/dt|_{\text{Transf}}$. This term will thus be studied in more detail in Section 3.6.

Unlike the jet simulation, the flux emergence simulations do not possess a quasi-ideal phase, and a finite level of nonideality is present as soon as the emerging flux rope enters in the coronal domain. This can be seen with non-null values of $dH_x/dt|_{\text{Diss}}$ and F_{Nonideal} presented in Figures 7 and 8 during the whole simulation. As expected, the intensity of these terms is very low. In other words, nonideal effects seem to have only a small impact on the temporal evolution of helicities.

A difference between the emergence simulations and the jet simulation is the mechanism by which magnetic energy and helicity accumulate in the system. In the jet simulation, helicity is inputted at the boundary by a purely rotational motion of a

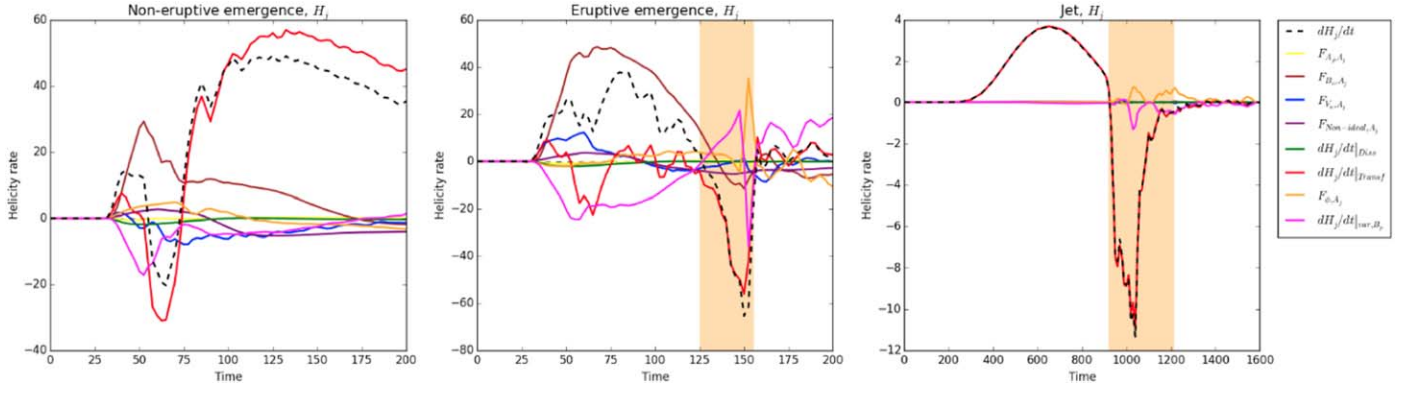


Figure 7. Time evolution of the nonpotential helicity variation rate (dashed black line; dH_j/dt ; Equation (28)) and the different terms constituting the instantaneous time variation of H_j (Equation (28)): F_{A_j, A_j} (yellow line; Equation (34)), F_{B_n, A_j} (brown line; Equation (33)) F_{V_n, A_j} (blue line; Equation (32)), $dH_j/dt|_{\text{Transf}}$ (red line; Equation (30)), F_{ϕ, A_j} (orange line; Equation (35)), $dH_j/dt|_{B_p, \text{var}}$ (magenta line; Equation (31)), F_{Nonideal, A_j} (purple line; Equation (56)), and $dH_j/dt|_{\text{Diss}}$ (green line; Equation (49)). From left to right: the noneruptive emergence simulation, the eruptive emergence simulation, and the simulation of the generation of a solar coronal jet. The yellow bands are the same as in Figure 3.

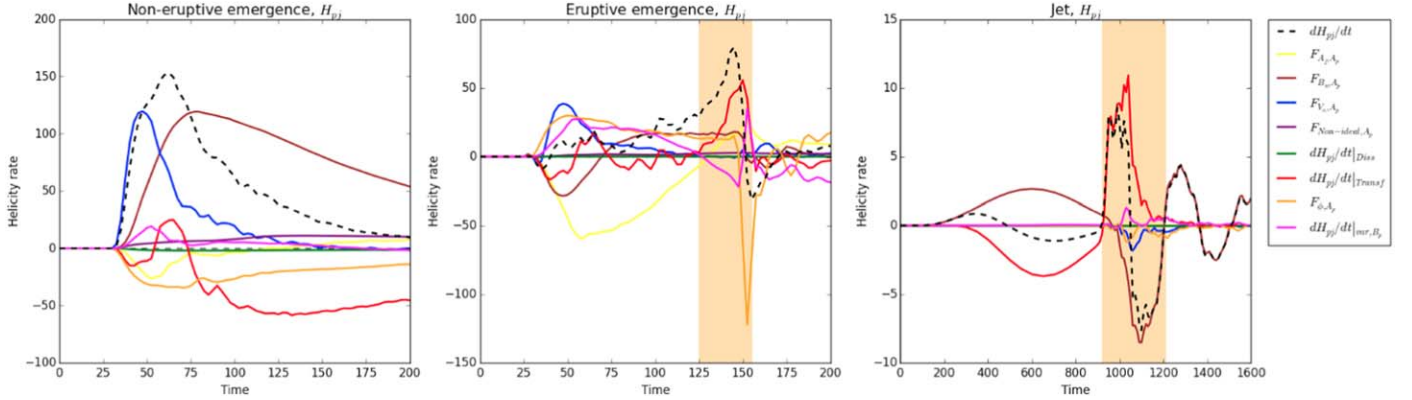


Figure 8. Time evolution of the volume-threading helicity variation rate (dashed black line; dH_{pj}/dt ; Equation (36)) and the different terms constituting the instantaneous time variation of H_{pj} (Equation (36)): F_{A_j, A_p} (yellow line; Equation (42)), F_{B_n, A_p} (brown line; Equation (41)) F_{V_n, A_p} (blue line; Equation (40)), $dH_{pj}/dt|_{\text{Transf}}$ (red line; Equation (38)), F_{ϕ, A_p} (orange line; Equation (43)), $dH_{pj}/dt|_{B_p, \text{var}}$ (magenta line; Equation (39)), F_{Nonideal, A_p} (purple line; Equation (56)), and $dH_{pj}/dt|_{\text{Diss}}$ (green line; Equation (54)). From left to right: the noneruptive emergence simulation, the eruptive emergence simulation, and the simulation of the generation of a solar coronal jet. The yellow bands are the same as in Figure 3.

symmetric field distribution that leaves the potential field unchanged. Here symmetry and flow geometry account for lots of cancellation. Because of this, all the surface terms F_{α, A_j} are almost null in the right panel of Figure 7. Only F_{ϕ, A_j} displays a weak variation during the jet, indicating the sudden load change of the reference magnetic field \mathbf{B}_p caused by the reconnections.

On the contrary, for the emergence simulations, A_j changes during the passage of the flux rope through the bottom boundary. This leads to significant contributions of the different flux terms during the pre-eruptive phase, as displayed by the evolution of the terms F_{V_n, A_j} and F_{B_n, A_j} . During the eruption, for the eruptive emergence simulation as with the jet case, the scalar potential ϕ changes abruptly, and therefore so do $dH_j/dt|_{B_p, \text{var}}$ and F_{ϕ, A_j} . It is a consequence of the boundary modification conditions for the Laplace equation due to the transit of eruption through the surface.

The flux F_{α, A_p} presented in Equation (36) depends not on A_j but on the vector potential A_p . For the emergence simulations, A_p changes significantly in emergence phase, yielding the dominant role of F_{B_n, A_p} and F_{V_n, A_p} .

3.6. Transfer between H_j and H_{pj}

Figures 9–11 show the time variation of H_j and H_{pj} in the gauge-invariant form of Equations (52) and (53) for the noneruptive flux emergence, the eruptive flux emergence, and the jet simulations, respectively. For the emergence simulations, the dissipation $dH_x/dt|_{\text{Diss}}$, which is explicitly calculated, is completely negligible compared to the two other terms. As mentioned in Section 3.5, nonideal terms are not null, but their intensity is very low. In the case of the relative magnetic helicity, a weak dissipation was sufficient to conclude that H_v is very well conserved (Pariat et al. 2015). This is not the case for H_j and H_{pj} because of the transfer term. Overall, in Figures 9–11 we observe that the volume transfer terms, $dH_x/dt|_{\text{Transf}}$, tend to have important values and frequently dominate the helicity variations. This is the key result of the analysis of these numerical simulations. As discussed earlier (see Section 2.4), these terms are pure volume terms. The presence of the transfer thus confirms that H_j and H_{pj} are not conserved quantities, unlike relative magnetic helicity, which is very well conserved for these simulations. Additionally, we observe that the dynamics of the helicity decomposition is often

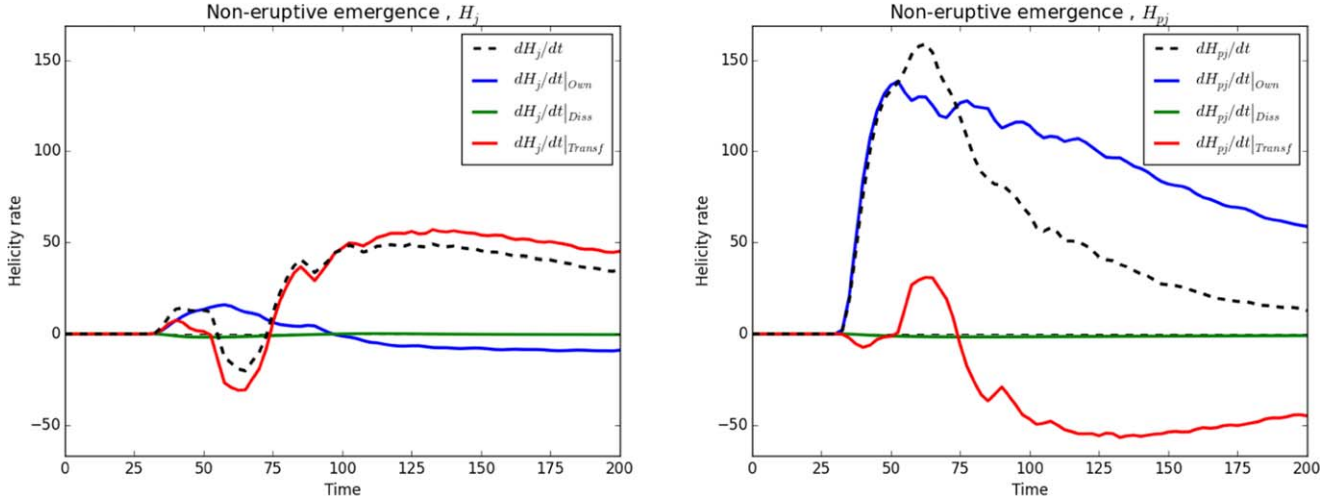


Figure 9. Time evolution of the helicity variation rates, dH_j/dt and dH_{pj}/dt (dashed black curves; Equations (28) and (36)), of the helicity transfer rates, $dH_j/dt|_{\text{Transf}}$ and $dH_{pj}/dt|_{\text{Transf}}$ (solid red curves; Equations (30) and (38)), of the “Own” rates, $dH_j/dt|_{\text{Own}}$ and $dH_{pj}/dt|_{\text{Own}}$ (solid blue curves; Equation (51) and (55)), and of the dissipation rates, $dH_j/dt|_{\text{Diss}}$ and $dH_{pj}/dt|_{\text{Diss}}$ (solid green curves; Equations (49) and (54)) for the noneruptive emergence simulation. The left and right panels present the evolution of the nonpotential helicity, H_j , and volume-threading helicity, H_{pj} , respectively.

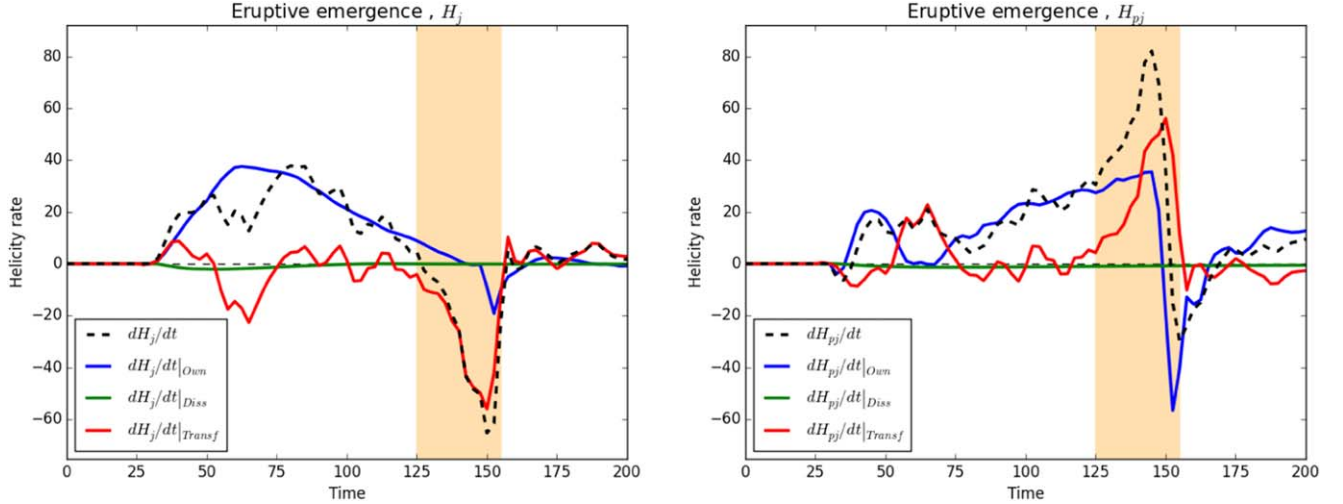


Figure 10. Same as Figure 9, but for the eruptive flux emergence simulation. The yellow bands correspond to the eruptive phase.

dominated by the exchange between H_j and H_{pj} , rather than their own fluxes through the volume boundaries. This is particularly true for H_j , for which the $dH_j/dt|_{\text{Own}}$ term is usually unimportant in two out of three cases. These results have important consequences for the estimation of H_j in the solar context, as will be discussed in Section 4.

Figures 9–11, along with Figure 3, allow us to follow the dynamics of the exchange between H_j and H_{pj} in the volume, as well as their exchange with the environment, in the different simulations. The noneruptive emergence case is the most straightforward to analyze. In the left panel of Figure 3, we distinguish two main behaviors: before $t \sim 80$, H_j is increasing along with H_{pj} , and after $t \sim 80$, H_j starts to grow. The intensity of H_{pj} is still increasing but is tending to a constant value. For $t \in [25, 80]$, corresponding to the emergence of the flux rope, we note in Figure 9 that $dH_{pj}/dt|_{\text{Own}}$ is the predominant flux (in particular owing to $F_{Vn,Ap}$ and $F_{Bn,Ap}$ in this gauge; Figure 8). During this period, H_j fluctuates weakly because of the exchange with H_{pj} (see left panel of Figure 3). Figure 9 (left panel) allows an additional understanding of

Figure 3: after $t \sim 80$, H_j is increasing not because of its flux through the surface but only as a result of the transfer term, $dH_j/dt|_{\text{Transf}}$. While $dH_{pj}/dt|_{\text{Own}}$ (see Figure 9, right panel) is still dominating the variation of H_{pj} , a large portion of it is directly transferred to H_j , thanks to the significant negative values of $dH_{pj}/dt|_{\text{Transf}}$. These oppositely signed terms partly balance each other and explain why the rise of H_{pj} is slower than before $t \sim 80$ (see Figure 3, left panel). We also note that $dH_j/dt|_{\text{Own}}$ is negligible during most of the simulation (left panel of Figure 9): the low fluctuations of this term may be related to the helicity measurement error $D_{n,j}$ (see Figure 4), which is relatively important before $t \sim 80$ (see Section 3.4).

The situation is more complicated for the eruptive emergence simulation. Indeed, $dH_j/dt|_{\text{Own}}$ presents a significant intensity during the whole simulation (see Figure 10). The “Own” terms could be due not only to emergence flows but also to the pervasive reconnection between the emerging flux and the coronal arcade fields. This reconnection starts as soon as the flux emerges through the photosphere. Thus, $dH_x/dt|_{\text{Own}}$ is more important than in the noneruptive simulation, where

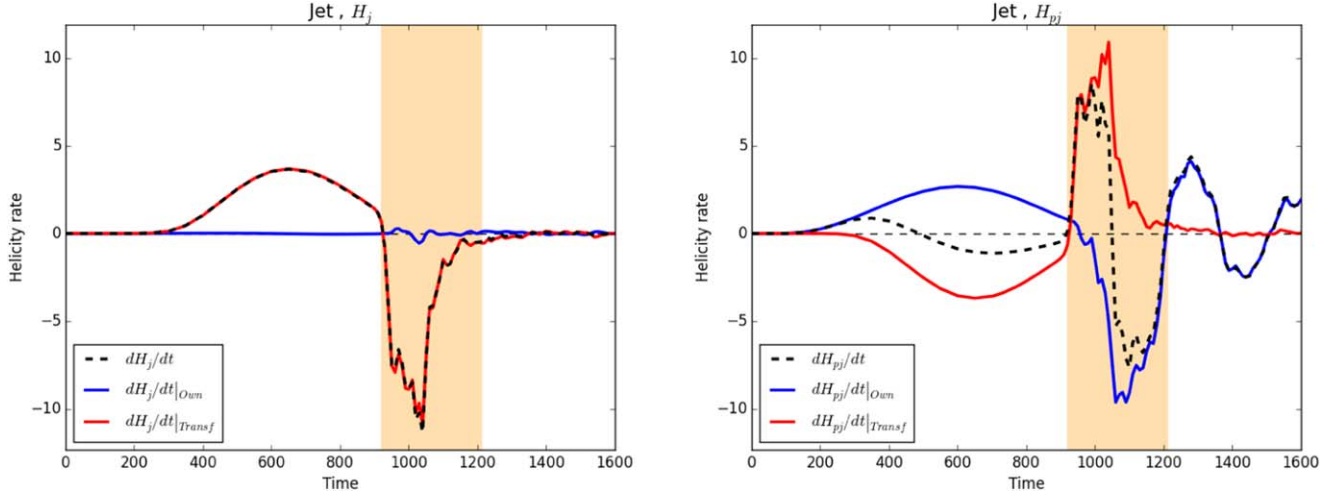


Figure 11. Same as Figure 9, but without the dissipation rates, $dH_j/dt|_{\text{Diss}}$ (Equation (49)) and $dH_{pj}/dt|_{\text{Diss}}$ (Equation (54)). For this simulation, these terms are assumed to be null. The yellow bands correspond to the jet eruption phase.

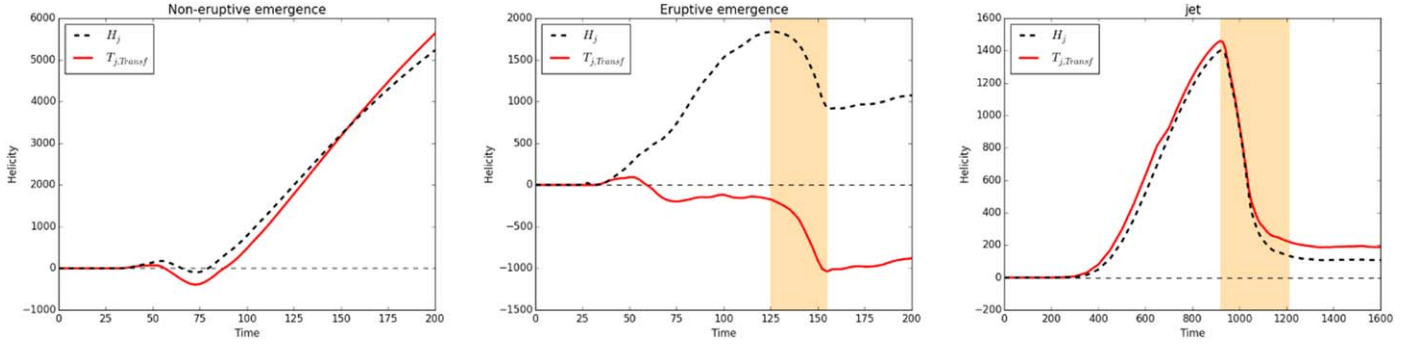


Figure 12. Time evolution of the nonpotential helicity H_j (dashed line; Equation (6)) and the time integral of the transfer rate $T_{j,\text{Transf}}$ (red lines; Equation (69)) for the noneruptive emergence simulation (left panel), the eruptive emergence simulation (middle panel), and the simulation of the generation of a solar coronal jet (right panel). The yellow vertical bands are the same as in Figure 3.

there is less reconnection early on and where the “Own” terms are likely due to the surface flows.

In Figure 10, after $t \sim 75$, the $dH_x/dt|_{\text{Own}}$ terms are higher than the transfer term, $dH_j/dt|_{\text{Transf}}$. The transfer term is weaker and hovers around zero during most of the pre-eruptive phase. Suddenly, after $t \sim 150$, $dH_j/dt|_{\text{Transf}}$ becomes negative and dominant. While H_j decreases (see Figure 3, middle panel), H_{pj} increases quickly because of the conversion of H_j . Consequently, H_v still increases. However, after $t \sim 150$, H_{pj} decreases because of the ejection of the magnetic structure through the top boundary (and consequently a decrease of H_v is observed). We observe in Figure 10, as indicated by the dominant values of $dH_j/dt|_{\text{Transf}}$ during the eruption phase, that the nonpotential helicity H_j is not directly expelled through the system boundaries: during the eruption phase, it is first transformed into H_{pj} . This quantity is then ejected outside, around $t \sim 150$, as seen by a negative peak of $dH_{pj}/dt|_{\text{Own}}$. Overall, Figure 10 explains why the decrease of H_j and H_v shows a delay with the decrease of H_j during the eruption (as seen in Figure 3, middle panel).

In the jet simulation, the energy and helicity do not increase in the volume by the emergence of a magnetic structure, but by the boundary shearing motions. During the whole ideal phase, before $t \sim 920$, $dH_j/dt|_{\text{Own}}$ is negligible. The injection of helicity from the external domain is primarily provided by the flux of H_{pj} (thanks to $F_{\text{Bn,Ap}}$ in the gauge used in this paper; see

Figure 8): only H_v and H_{pj} increase before $t \sim 350$ (see Figure 3, right panel). While initially $dH_{pj}/dt|_{\text{Own}}$ dominates $dH_j/dt|_{\text{Transf}}$, very rapidly the situation changes: $dH_j/dt|_{\text{Transf}}$ becomes the dominant term and dH_{pj}/dt becomes negative after $t \sim 500$ (see Figure 11, right panel), H_{pj} decreases to the benefit of H_j . In Figure 3, we see that H_v is increasing along with H_j , and that H_{pj} decreases. Without the analysis of Figure 11, one could imagine, when observing the right panel of Figure 3, that H_v is increasing directly owing to the injection of H_j . However, the situation is more complex. Because of the injection of currents, the increase of H_v is still due to an injection of H_{pj} through the boundary; however, a conversion from H_{pj} to H_j is occurring simultaneously at an even higher rate, as shown by the dominant values of $dH_j/dt|_{\text{Transf}}$ (see Figure 11). Hence, in Figure 3 (right panel), H_{pj} decreases and both H_j and H_v increase. At the moment of the jet, after $t \sim 920$, we find again the same behavior as during the eruptive emergence simulation: a fast transfer of H_j to H_{pj} directly followed by ejection of H_{pj} through the boundaries, as indicated by the succession of a positive peak of $dH_{pj}/dt|_{\text{Transf}}$ followed by a negative peak of $dH_{pj}/dt|_{\text{Own}}$ (see Figure 11, right panel). This conversion seems to be a marker of the beginning of eruptive activity.

Overall, the analysis of the evolution of the terms of the helicity decomposition in the three simulations shows that the flux H_j from outside of the system, $dH_j/dt|_{\text{Own}}$, is either

positive or negligible compared to the transfer term. In that respect, while the increase of the nonpotential helicity can be due to its own flux, the decrease of H_j seems to be mainly related to its conversion to H_{pj} . Moreover, this transfer (probably related to the ongoing magnetic reconnections) appears as the first phase of an eruption.

As discussed before, $dH_j/dt|_{\text{Transf}}$ frequently dominates the variation of H_j , during either the non-/pre-eruptive or eruptive phases. To highlight its impact on the evolution of H_j , Figure 12 presents the time integral, $T_{j,\text{Transf}}$, of the transfer term:

$$\begin{aligned} T_{j,\text{Transf}} &= \int^t \frac{dH_j}{dt'} \Big|_{\text{Transf}} dt' \\ &= -2 \int^t \int_V ((\mathbf{v} \times \mathbf{B}) \cdot \mathbf{B}_p) dV dt'. \end{aligned} \quad (69)$$

As can be seen in the right panel of Figure 12, for the jet simulation, the behaviors of $T_{j,\text{Transf}}$ and H_j are very similar: the curves overlap with only a small deviation toward the end of the simulation. The same is also true for the noneruptive emergence simulation (see Figure 12, left panel). This result is the direct consequence of the relatively low value of $dH_j/dt|_{\text{Own}}$ for these two simulations (see Figures 9 and 11, left and right panels). The evolution of H_j in these two cases is directly related to its conversion from H_{pj} . In the eruptive emergence simulation in Figure 10, the term $dH_j/dt|_{\text{Own}}$ is not negligible compared to the transfer term. Consequently, in the middle panel of Figure 12, $T_{j,\text{Transf}}$ does not overlap with H_j . In other words, H_j cannot be computed by only considering the integral of the transfer term, which is what was expected if one only looks at the jet and noneruptive simulations. However, $T_{j,\text{Transf}}$ also allows us to locate the eruption, as can be done with H_j . The instant $t \sim 125$, where H_j decreases, exactly coincides with the main drop of the transfer term. This confirms that H_j losses are linked to a conversion toward H_{pj} .

4. Conclusion

The present work focused on the analytical and numerical study of time variations of the terms in the decomposition of relative magnetic helicity, H_v , into the sum of the current-carrying helicity, H_j , and the volume-threading helicity, H_{pj} . After having introduced the different quantities, we analytically derived their time derivatives (see Section 2). We obtained the generalized equations for the time variation of H_j (see Equation (28)) and H_{pj} (see Equation (36)). We considered special cases and gauge choices that can simplify the calculation of these formulae (see Section 2.5).

The key outcome of our analytical derivation was to reveal a gauge-invariant quantity that controls the transfer of helicity between H_j and H_{pj} , themselves gauge invariant ($dH_j/dt|_{\text{Transf}}$; see Equation (30)). Since this quantity is expressed with a volume term, we deduce that neither H_j nor H_{pj} is a conserved quantity in resistive or ideal MHD. While relative magnetic helicity can be built as an invariant quantity in ideal MHD, helicity can nonetheless be exchanged between H_j and H_{pj} , and the latter quantities evolve even by ideal MHD motions.

The time evolution of H_v , H_j , and H_{pj} and the terms entering in their time derivatives were then studied in three 3D MHD numerical simulations of solar coronal events (see Section 3.1): the generation of a coronal jet (Pariat et al. 2009), the formation of a stable active region by flux emergence (Leake et al. 2013), and the formation of an

eruptive active region (Leake et al. 2014). These simulations present a sample of boundary forcing (line-tied vs. flux emergence), as well as dynamics, e.g., ideal evolution, magnetic reconnection, and eruptions.

The analysis of these numerical experiments allowed us first to confirm numerically the time variation equations of H_j and H_{pj} that were derived analytically (see Section 3.2). This confirms, evidently in some cases, that H_j and H_{pj} are not individually invariants of ideal MHD.

In particular, we observed that in many cases the transfer term $dH_j/dt|_{\text{Transf}}$ was dominating the dynamics of H_j (see Section 3.6). We observed that the evolution of H_j is frequently uniquely controlled by the term $dH_j/dt|_{\text{Transf}}$, which means that this quantity does not evolve as a result of boundary fluxes but builds up through the transformation of H_{pj} . This dynamics was observed both during the energy buildup phases of the evolution of the system and during the eruption/ejection phases. During the energy injection phases, for both the jet and the stable emergence simulations, boundary fluxes first increase H_{pj} , and part of it is then transformed into H_j . During the eruption phases (in the jet and eruptive emergence simulations), H_j is first transformed into H_{pj} , and it is the latter that is expelled from the domain by boundary fluxes.

This finding has an important impact on our ability to estimate H_j and H_{pj} in observed solar active regions. As discussed in Section 1, the most common way to estimate relative magnetic helicity is by time integration of its flux through the solar photosphere. Since relative magnetic helicity is largely conserved, its photospheric flux dominates the evolution of the relative helicity in the coronal domain. From numerical simulations, it was shown that indeed the time-integrated boundary fluxes closely match the amount of helicity in the system (Yang et al. 2013; Pariat et al. 2015, 2017). Lim et al. (2007) also confirmed from observational data that the helicity flux accumulation indeed gives a proper estimation of the coronal helicity with a $\sim 15\%$ relative error. However, such a flux-integration approach is doomed to fail when applied to H_j and H_{pj} . Indeed, the volume transfer term, which drives the evolution of H_j and H_{pj} , is independent of the boundary fluxes. In the jet simulation, for example, the time integration of the term $dH_j/dt|_{\text{Own}}$ is an order of magnitude smaller than the amount of H_j in the system. The analysis of H_j and H_{pj} in observations thus has to rely on the volume integration approach (Valori et al. 2016). In this method, the 3D coronal magnetic field must be reconstructed from the 2D photospheric measurements, thanks to extrapolation techniques (Wiegmann & Sakurai 2012; Wiegmann et al. 2014). Because of the inherent nature of H_j , which describes nonpotential fields, potential magnetic field reconstruction cannot estimate this quantity. Similarly, we believe that linear force-free extrapolation will only provide too crude an approximation of H_j . The linear force-free approximation can be used to estimate relative helicity solely thanks to the boundary distribution of the normal component of the magnetic field (Berger 1985; Lim et al. 2007). The impact of this approximation on the estimation of H_j and H_{pj} remains to be studied, but it can be conjectured that, since the linear approximation effectively distributes current in the entire volume, it is inaccurate for systems, like the corona, where currents are spatially localized. These quantities being highly nonlinear, non-force-free extrapolations will probably be a unique way to properly approach an estimation of H_j and H_{pj} , similarly to the study of James et al. (2018), who provided the first estimation of H_j/H_v in observed data.

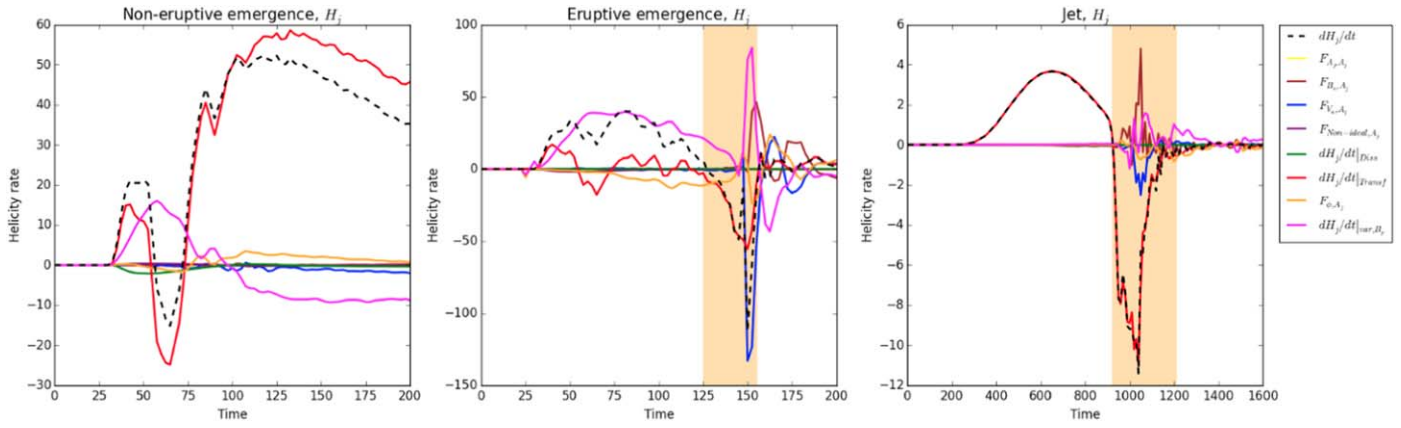


Figure 13. Same as Figure 7, but using condition (70) instead of condition (66).

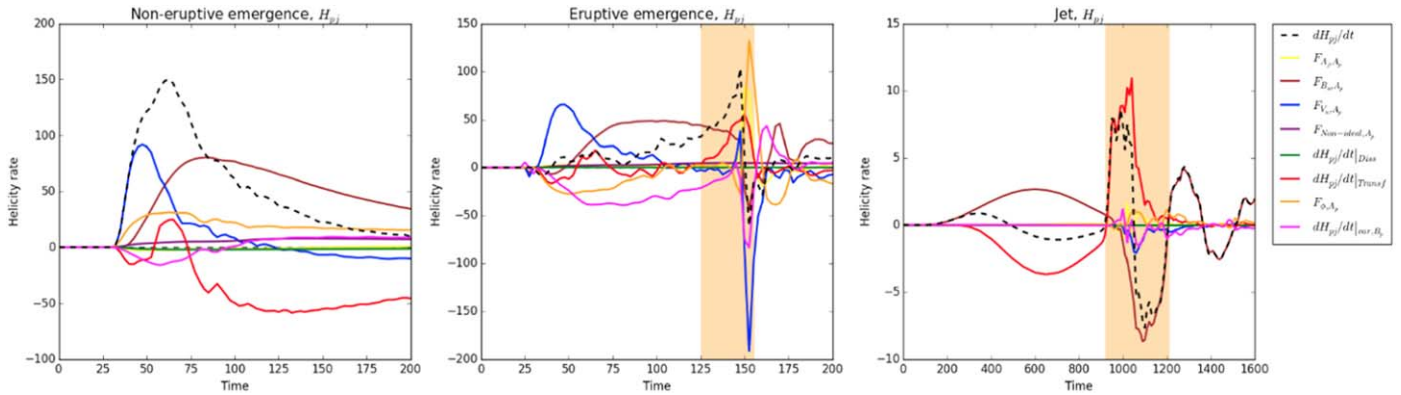


Figure 14. Same as Figure 8, but using condition (70) instead of condition (66).

Pariat et al. (2017) and Zuccarello et al. (2018) have shown that the helicity ratio H_j/H_v seems to be tightly related to the eruption process. This paper presents an additional evidence through the analysis of the coronal jet simulation of Pariat et al. (2009). We show here that the jet is indeed triggered when the helicity ratio H_j/H_v attains a very high value. The value of this ratio drops significantly after the generation of the jet. If, as hinted by these studies, H_j is a key element for the eruptivity of solar active regions, the present study demonstrates the need for the development of quality 3D magnetic reconstructions of the solar magnetic field in order to measure H_j and H_{pj} in observed solar active regions. The *Solar Orbiter* mission and its PHI instrument, which will provide the first remote magnetic field observations complementing those from the Earth environment, may provide a unique opportunity to improve vector magnetic field measurements. Finally, the present work has highlighted yet another interesting behavior of magnetic helicity. The nonpotential helicity H_j evolution seems to be mostly driven by the volume transformation from H_{pj} rather than from its own flux. Further investigations on different magnetic field simulations are required to capture the dynamics of this quantity. More generally, magnetic helicity needs to be further understood through fundamental studies on its mathematical properties (Oberti & Ricca 2018), on its physical interpretation (Yeates & Hornig 2013, 2014; Russell et al. 2015; Aly 2018), and on its proper measurement in the solar corona (Dalmasse et al. 2013, 2014, 2018; Valori et al. 2016; Guo et al. 2017; Moraitis et al. 2018).

The authors thank the anonymous reviewer for careful reading of the manuscript. L.L., E.P., and K.M. acknowledge

the support of the French Agence Nationale pour la Recherche through the HELISOL project, contract No. ANR-15-CE31-0001. G.V. acknowledges the support of the Leverhume Trust, Research Project Grant 2014-051. J.L. is supported by NASA's LWS and HGI programs. The authors acknowledge access to the HPC resources of CINES under the allocations 2017-046331 made by GENCI (Grand Equipement National de Calcul Intensif).

Appendix Helicity Variation Decomposition with a Different Gauge Choice

In the core part of this study, in our application of the helicity estimation to numerical experiments (see Section 3), we used the practical DeVore–Coulomb gauge for \mathbf{A} and \mathbf{A}_p , with the additional constraint that they have the same distribution at the top boundary (see condition (66)). This choice induces that all the fluxes F_{α, A_j} (with $\alpha \in \{V_n, B_n, A_j, \phi\}$) in Equation (28) are null at the top boundary. To determine the impact of this choice, we perform the helicity calculations with a different condition:

$$\mathbf{A}(x, y, z = z_{\text{bot}}, t)_{\perp} = \mathbf{A}_p(x, y, z = z_{\text{bot}}, t)_{\perp}, \quad (70)$$

i.e., with \mathbf{A} and \mathbf{A}_p having the same distribution at the bottom boundary, at $z = z_{\text{bot}}$, instead of the top boundary.

All the helicity evaluations performed in Section 3 are recomputed with this new gauge choice. We only present here the results in which the gauge choice has a significant impact. As expected, all the gauge-independent quantities are not affected by the switch between conditions (66) and (70). Only the figures

presenting gauge-dependent quantities are significantly affected, those representing the different terms in the helicity time variations of Equations (28) and (36). These terms, computed with condition (70), are presented in Figures 13 and 14. These figures should be compared with Figures 7 and 8 (see Section 3.5).




As expected, the curves in Figure 13 (Figure 14) are markedly different from the curves in Figure 7 (Figure 8). Indeed, the fluxes in Equations (28) and (36) are gauge dependent (see Section 2.4.2). Only the term $dH_x/dt|_{\text{Transf}}$ is gauge invariant and is strictly identical. We also note that $\Delta H_j/\Delta t$ and $\Delta H_{pj}/\Delta t$ are almost identical, the marginal difference (<4%) being due to the intrinsic precision on the estimation of the helicities due to the finite nonsolenoidality of the data sets (see Sections 3.1).

For the jet simulation (right panel of Figure 13), the differences appear mainly during the nonideal phase (after $t \sim 900$). During that phase, a jet and a nonlinear magnetic wave are passing through the top boundary. Hence, the magnetic and the velocity fields vary significantly at the top boundary. Since with condition (66) $F_{\text{Bn,Aj}}$ and $F_{\text{Vn,Aj}}$ are constantly null at the top boundary, these quantities presented very weak values in Figure 7 (right panel) during the passage of the jet. The top constraint being lifted with condition (70), $F_{\text{Bn,Aj}}$ and $F_{\text{Vn,Aj}}$ show significantly large values in Figure 13 around $t \sim 1000$. The different boundary fluxes nonetheless cancel each other, and the gauge-independent quantity $dH_j/dt|_{\text{Own}}$ remains very low (as in Figure 11), significantly smaller than $dH_j/dt|_{\text{Transf}}$.

For the noneruptive and eruptive emergence simulations, before $t \sim 120$, with condition (70) the contributions of $F_{\text{Vn,Aj}}$ and $F_{\text{Bn,Aj}}$ have completely disappeared (see Figure 13). These quantities depend mostly on the change of the velocity and magnetic fields at the bottom boundary while the flux tube was emerging. With the vector potential A_j being forced to be null at this boundary, the fluxes are null as well. The quantity dH_j/dt evolves almost only thanks to the volume terms: the transfer term and $dH_j/dt|_{\text{BP,var}}$. With this particular gauge choice H_j does not exchange with the outside during the pre-eruptive phase, for both the eruptive and the noneruptive simulations.

During the eruptive phase of the eruptive emergence simulation (middle panels of Figures 13 and 14), we see that $F_{\text{Vn,Ax}}$, with x being either j or pj , is the main contribution of the helicity fluxes. The computations of $D_{n,x}$ (Equation (68)) and $dH_x/dt|_{\text{Own}}$ (not shown here) inform us that this peak of $F_{\text{Vn,Aj}}$ is likely due to numerical errors: the time step is not sufficiently small to capture the sudden change of the velocity field at the top boundary. At that particular time the computation method and the specific choice of gauge can markedly influence the precision of the helicity flux estimation. These results had already been noted by Pariat et al. (2015, 2017).

ORCID iDs

É. Pariat  <https://orcid.org/0000-0002-2900-0608>
 G. Valori  <https://orcid.org/0000-0001-7809-0067>
 J. Leake  <https://orcid.org/0000-0002-6936-9995>

References

Aly, J.-J. 2018, *FIDyR*, 50, 011408
 Antiochos, S. K. 2013, *ApJ*, 772, 72
 Berger, M. A. 1985, *ApJS*, 59, 433

Berger, M. A. 2003, in *Advances in Nonlinear Dynamos*, ed. A. Ferriz-Mas & Manuel Núñez (Boca Raton, FL: CRC Press), 345
 Berger, M. A., & Field, G. B. 1984, *JFM*, 147, 133
 Brandenburg, A., Petrie, G. J. D., & Singh, N. K. 2017, *ApJ*, 836, 21
 Brandenburg, A., & Subramanian, K. 2005, *PhR*, 417, 1
 Burlaga, L. F. 1995, in *Int. Ser. in Astronomy and Astrophysics*, Vol. 3, *Interplanetary Magnetohydrodynamics* (Oxford: Oxford Univ. Press)
 Candelaresi, S. 2012, PhD thesis, Stockholm Univ. (<http://www.maths.dundee.ac.uk/scandelaresi/publications/theses/PhDthesis.pdf>)
 Chae, J. 2001, *ApJL*, 560, L95
 Chae, J. 2007, *AdSpR*, 39, 1700
 Dalmasse, K., Pariat, E., Démoulin, P., & Aulanier, G. 2014, *SoPh*, 289, 107
 Dalmasse, K., Pariat, E., Valori, G., Démoulin, P., & Green, L. M. 2013, *A&A*, 555, L6
 Dalmasse, K., Pariat, E., Valori, G., Jing, J., & Démoulin, P. 2018, *ApJ*, 852, 141
 Dasso, S. 2009, in *IAU Symp. Vol. 257, Universal Heliophysical Processes* (Cambridge: Cambridge Univ. Press), 379
 Dasso, S., Mandrini, C. H., Démoulin, P., & Farrugia, C. J. 2003, *JGRA*, 108, 1362
 Dasso, S., Mandrini, C. H., Démoulin, P., Luoni, M. L., & Gulisano, A. M. 2005, *AdSpR*, 35, 711
 Del Sordo, F., Candelaresi, S., & Brandenburg, A. 2010, *PhRvE*, 81, 036401
 Démoulin, P. 2007, *AdSpR*, 39, 1674
 Démoulin, P. 2008, *AnGeo*, 26, 3113
 Démoulin, P., Janvier, M., & Dasso, S. 2016, *SoPh*, 291, 531
 Démoulin, P., & Pariat, E. 2009, *AdSpR*, 43, 1013
 Démoulin, P., Pariat, E., & Berger, M. A. 2006, *SoPh*, 233, 3
 DeVore, C. R. 2000, *ApJ*, 539, 944
 Elsässer, W. M. 1956, *RvMP*, 28, 135
 Finn, J. H., & Antonsen, T. M. J. 1985, *CoPPC*, 9, 111
 Georgoulis, M. K., Tziotziou, K., & Raouafi, N.-E. 2012, *ApJ*, 759, 1
 Guennou, C., Pariat, E., Leake, J. E., & Vilmer, N. 2017, *JSWSC*, 7, A17
 Guo, Y., Ding, M.-D., Cheng, X., Zhao, J., & Pariat, E. 2013, *ApJ*, 779, 157
 Guo, Y., Ding, M.-D., Schmieder, B., et al. 2010, *ApJL*, 725, L38
 Guo, Y., Pariat, E., Valori, G., et al. 2017, *ApJ*, 840, 40
 Hu, Q., Qiu, J., Dasgupta, B., Khare, A., & Webb, G. M. 2014, *ApJ*, 793, 53
 James, A. W., Valori, G., Green, L. M., et al. 2018, arXiv:1802.07965
 Kazachenko, M. D., Canfield, R. C., Longcope, D. W., et al. 2009, *ApJ*, 704, 1146
 Kazachenko, M. D., Canfield, R. C., Longcope, D. W., & Qiu, J. 2010, *ApJ*, 722, 1539
 Kazachenko, M. D., Canfield, R. C., Longcope, D. W., & Qiu, J. 2012, *SoPh*, 277, 165
 Knizhnik, K. J., Antiochos, S. K., & DeVore, C. R. 2015, *ApJ*, 809, 137
 Kusano, K., Maeshiro, T., Yokoyama, T., & Sakurai, T. 2004, *ApJ*, 610, 537
 Leake, J. E., Linton, M. G., & Antiochos, S. K. 2014, *ApJ*, 787, 46
 Leake, J. E., Linton, M. G., & Török, T. 2013, *ApJ*, 778, 99
 Lim, E.-K., Jeong, H., Chae, J., & Moon, Y.-J. 2007, *ApJ*, 656, 1167
 Linton, M. G., & Antiochos, S. K. 2002, *ApJ*, 581, 703
 Linton, M. G., Dahlburg, R. B., & Antiochos, S. K. 2001, *ApJ*, 553, 905
 Liu, Y., & Schuck, P. W. 2012, *ApJ*, 761, 105
 Liu, Y., & Schuck, P. W. 2013, *SoPh*, 283, 283
 Longcope, D. W., & Beveridge, C. 2007, *ApJ*, 669, 621
 Longcope, D. W., Ravindra, B., & Barnes, G. 2007, *ApJ*, 668, 571
 Low, B. C. 1996, *SoPh*, 167, 217
 Low, B. C. 2006, *ApJ*, 646, 1288
 Luoni, M. L., Mandrini, C. H., Dasso, S., van Driel-Gesztelyi, L. L., & Démoulin, P. 2005, *JATP*, 67, 1734
 Mandrini, C. H., Pohjolainen, S., Dasso, S., et al. 2005, *A&A*, 434, 725
 Miesch, M. S., Zhang, M., & Augustson, K. C. 2016, *ApJL*, 824, L15
 Moffatt, H. K. 1969, *JFM*, 35, 117
 Moraitis, K., Pariat, E., Savcheva, A., & Valori, G. 2018, *SoPh*, 293, 92
 Moraitis, K., Tziotziou, K., Georgoulis, M. K., & Archontis, V. 2014, *SoPh*, 289, 4453
 Oberti, C., & Ricca, R. L. 2018, *FIDyR*, 50, 011413
 Pariat, E., Antiochos, S. K., & DeVore, C. R. 2009, *ApJ*, 691, 61
 Pariat, E., Dalmasse, K., DeVore, C. R., Antiochos, S. K., & Karpen, J. T. 2016, *A&A*, 596, A36
 Pariat, E., Démoulin, P., & Berger, M. A. 2005, *A&A*, 439, 1191
 Pariat, E., Leake, J. E., Valori, G., et al. 2017, *A&A*, 601, A125
 Pariat, E., Valori, G., Démoulin, P., & Dalmasse, K. 2015, *A&A*, 580, A128
 Patsourakos, S., & Georgoulis, M. K. 2017, *SoPh*, 292, 89
 Patsourakos, S., Georgoulis, M. K., Vourlidis, A., et al. 2016, *ApJ*, 817, 14
 Polito, V., Del Zanna, G., Valori, G., et al. 2017, *A&A*, 601, A39

- Priest, E. R., Longcope, D. W., & Janvier, M. 2016, [SoPh](#), **291**, 2017
- Rudenko, G. V., & Myshyakov, I. I. 2011, [SoPh](#), **270**, 165
- Russell, A. J. B., Yeates, A. R., Hornig, G., & Wilmot-Smith, A. L. 2015, [PhPI](#), **22**, 032106
- Rust, D. M. 1994, [GeoRL](#), **21**, 241
- Taylor, J. B. 1974, [PhRvL](#), **33**, 1139
- Temmer, M., Thalmann, J. K., Dissauer, K., et al. 2017, [SoPh](#), **292**, 93
- Thalmann, J. K., Inhester, B., & Wiegelmann, T. 2011, [SoPh](#), **272**, 243
- Valori, G., Démoulin, P., & Pariat, E. 2012, [SoPh](#), **278**, 347
- Valori, G., Démoulin, P., Pariat, E., & Masson, S. 2013, [A&A](#), **553**, 38
- Valori, G., Pariat, E., Anfinogentov, S., et al. 2016, [SSRv](#), **201**, 147
- Webb, G. M., Hu, Q., Dasgupta, B., & Zank, G. P. 2010, [JGRA](#), **115**, A10112
- Webb, G. M., Hu, Q., Dasgupta, B., & Zank, G. P. 2011, [JGRA](#), **116**, A11102
- Wiegelmann, T., & Sakurai, T. 2012, [LRSP](#), **9**, 5
- Wiegelmann, T., Thalmann, J. K., & Solanki, S. K. 2014, [A&ARv](#), **22**, 78
- Woltjer, L. 1958, [PNAS](#), **44**, 489
- Yang, S., Büchner, J., Santos, J. C., & Zhang, H. Q. 2013, [SoPh](#), **283**, 369
- Yeates, A. R., & Hornig, G. 2013, [PhPI](#), **20**, 012102
- Yeates, A. R., & Hornig, G. 2014, [JPhCS](#), **544**, 012002
- Zhao, L., DeVore, C. R., Antiochos, S. K., & Zurbuchen, T. H. 2015, [ApJ](#), **805**, 61
- Zuccarello, F. P., Aulanier, G., & Gilchrist, S. A. 2015, [ApJ](#), **814**, 126
- Zuccarello, F. P., Pariat, E., Valori, G., & Linan, L. 2018, [ApJ](#), **863**, 41